Computational Materials Science 220 (2023) 112057

Contents lists available at ScienceDirect

Computational Materials Science

journal homepage: www.elsevier.com/locate/commatsci

Full length article

# Automated determination of grain boundary energy and potential-dependence using the OpenKIM framework

Brendon Waters [a], Daniel S. Karls [a], Ilia Nikiforov [a], Ryan S. Elliott [a], Ellad B. Tadmor [a], Brandon Runnels [b,*]

[a] Department of Aerospace Engineering and Mechanics, University of Minnesota, Minneapolis, MN, USA
[b] Department of Mechanical and Aerospace Engineering, University of Colorado, Colorado Springs, CO, USA

ARTICLE INFO

Dataset link: https://openkim.org/

*Keywords:*
Grain boundaries
Molecular dynamics
Interatomic potentials

ABSTRACT

We present a systematic methodology, built within the Open Knowledgebase of Interatomic Models (OpenKIM) framework (https://openkim.org), for quantifying properties of grain boundaries (GBs) for arbitrary interatomic potentials (IPs), GB character, and lattice structure and species. The framework currently generates results for symmetric tilt GBs in cubic materials, but can be readily extended to other types of boundaries. In this paper, GB energy data are presented that were generated automatically for Al, Ni, Cu, Fe, and Mo with 225 IPs; the system is installed on openkim.org and will continue to generate results for all new IPs uploaded to OpenKIM. The results from the atomistic calculations are compared to the lattice matching model, which is a semi-analytic geometric model for approximating GB energy. It is determined that the energy predicted by all IPs (that are stable for the given boundary type) correlate closely with the energy from the model, up to a multiplicative factor. It thus is concluded that the qualitative form of the GB energy versus tilt angle is dominated more by geometry than the choice of IP, but that the IP can strongly affect the energy level. The spread in GB energy predictions across the ensemble of IPs in OpenKIM provides a measure of uncertainty for GB energy predictions by classical IPs.

## 1. Introduction

As exploration of the behavior of materials progresses towards ever smaller scales, the influence of grain boundaries (GBs) on their mechanical properties has become increasingly relevant. In particular, the phenomenon of GB anisotropy, the dependence of GB excess energy [1] on the relative crystallographic orientation of the two adjacent grains, has been identified as a non-trivial effect in processes such as plasticity [2], twinning and phase transformation [3], and solidification [4]. However, while the orientation relationship between the grains (embodied in the coincident site lattice and $\Sigma$ value of the boundary) was originally thought to be predominant in determining the energy of a GB [5], it has become clear that it is strongly dependent upon the interface inclination, as well. That is, it has been shown that the excess energy exhibits a marked dependence upon all five microscopic degrees of freedom that define a GB [6,7], which we collectively refer to as its *character*.

Because of the eminent role played by GBs in micromechanics, and because a knowledge of their stability will be critical in developing methods for GB engineering [8], it is necessary to gather accurate data that relates the excess energy of a GB to its character. Grain boundaries have been a subject of study for many decades. The seminal analysis of GB energy as a function of misorientation was by Read [9], resulting in the well-known Read–Shockley equation. This was followed by insights from other investigators, such as the Frank–Bilby equation [10] and the O-Lattice model [11], all of which are restricted to GBs that are interpretable as arrays of geometrically necessary dislocations. For the general case, many attempts have been made to capture GB behavior accurately at all points in GB character space by means of analytical or semi-analytical models. Some methods, such as that of Bulatov et al. [12], rely on an interpolation-based approach for constructing a model informed by GB data [13] that reproduces the dependence of excess energy on orientation over a wide range of known GB configurations. It has also been argued in [12] that a geometry or crystallography-driven method is sufficient for approximating GB energy up to a scaling factor. Udler and Seidman suggested that GB energy scales with elastic moduli, implying a possible relationship; however, this has yet to be verified [14]. In a similar vein, some machine learning models (as well as potentials [15]) have proven useful in estimating GB energy [16,17], although their ability to predict irregular GB energy features is debatable.

* Corresponding author.
*E-mail address:* brunnels@uccs.edu (B. Runnels).

https://doi.org/10.1016/j.commatsci.2023.112057
Received 22 December 2022; Received in revised form 24 January 2023; Accepted 25 January 2023
Available online 9 February 2023

Advances from focused ion beam tomography (FIB) [18] to non-destructive full 3D tomography [19] provide a means for determining the effect of GB energy on microstructural evolution. However, aside from a modest collection of observations of excess energy for specific subsets of GB character [20,21], experimental data is scarce. The lack of experimental GB energy data has been mitigated to some extent by advancements in computational hardware that have made it possible to perform realistic atomistic simulations of GBs with sufficient complexity to determine energetic trends. Due to the computational cost, such simulations are typically performed using interatomic potentials (IPs): approximate functional forms fitted to ab initio and experimental data. IPs effect a significant reduction of order by solving only for atomic nuclei positions without resolving electron density. The resulting simulations are more computationally efficient, but require that the functional form and parameters of the IP be carefully selected.

Multiple wide-ranging atomistic studies of GB energy using IPs have been conducted. One of the first broad surveys was performed by Wolf [22–27], who considered symmetric and asymmetric tilt and twist boundaries in face-centered cubic (fcc) and body-centered cubic (bcc) materials. Still, exploration of GB energy for various materials, IPs, and crystal structures is a topic of ongoing research [28]. Of particular note are the evident similarities that have been identified between the relaxed GB energies of various materials with identical crystal lattice types, implying that their excess energy surfaces are the same up to a material-specific scaling constant [13].

Because the precise effect of IP choice on GB energy is generally missing from current GB studies, the primary contribution of this work is to specifically analyze the correlation, if any, between IPs and the relaxed GB energy they predict. Doing so requires a systematic framework for cataloging the massive sets of data that result from this broad sweep of possible GB character and, to this end, we leverage the Open Knowledgebase of Interatomic Models (OpenKIM, KIM) [29,30]. This system automates the process of computing the predictions of the many IPs stored within it by allowing users to upload atomistic simulation codes that calculate material properties of interest. We have developed this capability for computing the GB energy-versus-tilt angle relation for symmetric tilt GBs in cubic materials. In this article, we report on the results for aluminum (Al), nickel (Ni), copper (Cu), iron (Fe), and molybdenum (Mo) simulated using 225 IPs (as of December 2022). Additional results are continuously generated as IPs and material systems are added to OpenKIM, and current results are available online at https://openkim.org.

The remainder of this paper is structured as follows: Section 2 provides an overview of the OpenKIM framework as it relates to the problem of systematic GB energy calculations. Section 3 provides the details of the algorithm used to compute the GB energy and its implementation. In Section 4, results are presented and discussed for the above mentioned systems. The implications and limitations of the work are reviewed in Section 5.

## 2. The OpenKIM framework and grain boundary energy calculations

OpenKIM [29,30] is a cyberinfrastructure hosted at https://openkim.org for archiving computer implementations of IPs (referred to as *Models* in KIM terminology) and testing their predictions for different material properties. All KIM Models conform to an application programming interface (API) [31] that allows them to be used seamlessly and without alteration with a number of major simulation packages that conform to the KIM API (for a current list, see https://openkim.org/projects-using-kim). These Models are automatically coupled to a large number of "Tests" in the system that compute physical properties of interest. Some examples for crystalline systems are cohesive energy, equilibrium lattice constant, phonon dispersion, stacking fault energy, surface energy, thermal expansion, and vacancy formation energy. The Test–Model matching and calculation process is handled by the "KIM Processing Pipeline" [32,33], which creates corresponding jobs and distributes them to high-performance computing clusters whenever a new Model or Test is uploaded. To reduce compute time and promote reusable code, Tests can access the results of other Tests in the system for properties that they depend on, such as the equilibrium lattice constant of the crystal or its cohesive energy. These dependencies are handled automatically by the pipeline when determining the order in which sequences of Test–Model pairs are executed.

The results of all compatible Test–Model couplings run by the pipeline are stored online in the publicly accessible OpenKIM repository. These results can be viewed through a user-extendable visualization system integrated into the OpenKIM framework, as well as directly through standardized web queries [34]. This provides a wealth of information on the predictions of stored Models for a large number of material properties. New Models and Tests are uploadable by the user community, making the OpenKIM system an evolving, adaptive system.

An individual Test in the OpenKIM system is a fully specified calculation, e.g. the cohesive energy of Al in the fcc structure, or the (111) surface energy of Fe in the bcc structure. In practice, it is more efficient to work with "Test Drivers". Test Drivers are analogous to pure abstract classes in object oriented programming; they are designed to be as general as possible to reduce code redundancy. For example, a cohesive energy Test Driver could take in as input the crystal structure (lattice vectors, basis atoms, and species) and compute the energy-per-unit cell for this system for any Model with which it is coupled. Each set of inputs to the Test Driver then constitutes a Test. A Test Driver can be a stand-alone computer program written in any language supported by the KIM API (C, C++, Fortran 90 and greater) or can be a script that runs an external simulation code (called a "simulator" in KIM), such as the LAMMPS molecular dynamics (MD) package [35]. Consistent with this philosophy of modularity, KIM Models are handled similarly. An individual KIM Model may either consist of a self-contained program or as a parameter file that is read by a *Model Driver*.

To study GB energetics, we have developed a KIM Test Driver that computes the GB energy versus angle for symmetric tilt GBs in cubic materials [36] using LAMMPS. This Test Driver, and several dozen Tests which use it, are installed within the OpenKIM system and, as mentioned above, will therefore automatically be run with any new Models uploaded to the system. The specific algorithm used by the Test Driver to compute the tilt GB energy is described in the next section.

## 3. Symmetric tilt GB energy test driver algorithm

The symmetric tilt GB Test Driver reads in the species, crystal structure, tilt axis and range of tilt angles, a spatial resolution for the grid search over translations along the GB in units of the lattice constant of the material, and the maximum allowable length of any dimension of the periodic cell. Note that the interface inclination is not read in as a parameter because the current Test Driver is intended to model only symmetric tilt GBs. The equilibrium lattice constant and cohesive energy of the specified lattice are then automatically imported from the results of other Tests that were previously run against the IP being tested, as well as interatomic energies across a range of non-equilibrium lattice spacings (i.e. the cohesive energy versus lattice spacing curve), which are used to determine the minimum atomic separation where the interatomic energy of the lattice exceeds the single-atom energy. Any pairs of atoms in the initial unrelaxed GB configuration that are within this distance from a neighbor have one member automatically deleted to avoid unphysical configurations.[1] The following section describes the algorithm used in the Test Driver for constructing LAMMPS simulations.

[1] For a typical IP, the energy of a single isolated atom is zero, and hence the deletion criterion applies to pairs of atoms whose distance is less than the lattice constant at which the lattice energy becomes positive at short distances.

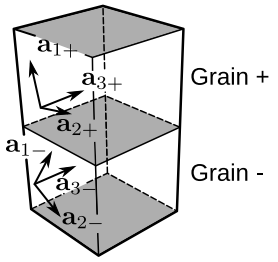


**Fig. 1.** Computational simulation domain for a symmetric tilt GB. Periodicity requires the creation of two GBs, the first of which is shown in the center and the second of which is formed by effectively adjoining the top and bottom of the simulation domain.

### 3.1. Definition of grain boundary excess energy

Following established definitions, (cf. [1,37–40]) we use the following definition for grain boundary excess energy between two grains, denoted "+" and "–"

$$\gamma = \lim_{L\to\infty} \frac{1}{L^2}\Big( \lim_{H\to\infty} \big(E_{\text{tot}}(\chi^+_{L,L,H}, \chi^-_{L,L,H}) - (N^+_{L,L,H} + N^-_{L,L,H})E_{\text{coh}}\big)\Big), \quad (1)$$

where $\chi^+_{L,L,H}, \chi^-_{L,L,H}$ are the relaxed atomic positions contained within the simulation domain, $[-\frac{L}{2},\frac{L}{2}]^2\times[-\frac{H}{2},\frac{H}{2}]$, and $N^+_{L,L,H}+N^-_{L,L,H}$ is the total number of atoms contained in the simulation domain. $E_{\text{coh}}$ is the cohesive energy of the crystals in their ground state. If the boundary is periodic within some finite cell, $[-\frac{L_1}{2},\frac{L_1}{2}]\times[-\frac{L_2}{2},\frac{L_2}{2}]$, the energy reduces to

$$\gamma = \frac{1}{L_1L_2}\Big( \lim_{H\to\infty} \big(E_{\text{tot}}(\chi^+_{L_1,L_2,H}, \chi^-_{L_1,L_2,H}) - (N^+_{L_1,L_2,H} + N^-_{L_1,L_2,H})E_{\text{coh}}\big)\Big). \quad (2)$$

In the limit as $H$ becomes large, then the energy is sufficiently approximated by

$$\gamma \approx \frac{1}{L_1L_2}\Big( E_{\text{tot}}(\chi^+_{L_1,L_2,H}, \chi^-_{L_1,L_2,H}) - (N^+_{L_1,L_2,H} + N^-_{L_1,L_2,H})E_{\text{coh}}\Big), \quad (3)$$

where $E_{\text{tot}}$ is computed via atomistic methods.

Nonnegativity of $\gamma$ requires that the first term in Eq. (3) be greater than the sum of the second two. $E_{\text{coh}}$ should be the energy per atom of the crystal in its optimal lattice configuration, guaranteeing that the boundary configuration will incur an increase of energy. However, if a cohesive energy for a higher-energy lattice configuration is chosen, e.g. a bcc cohesive energy used for a material with an fcc ground state, then the minimization may result in a phase transformation from the unstable lattice to the stable one. Such a configuration would result in a meaningless, possibly negative value of $\gamma$, and would be said to be an unstable configuration.

In the present work, GB energy computations are considered comprehensively for all IPs designed for a given material, regardless of actual ground state. As a result, several unstable configurations are included that may be systematically dismissed.

### 3.2. Domain generation

When setting up an atomistic GB simulation, a periodic computational representative domain is generally used. In order to respect this periodicity, a typical calculation of the GB energy necessitates the creation of two GBs (see Fig. 1). The algorithm implemented in the Test Driver for generating the repeating cell for a prescribed tilt angle is based on the significant body of work already done on the subject (see, for example, [41–43]). Let $\boldsymbol{g}_{1\pm}, \boldsymbol{g}_{2\pm}, \boldsymbol{g}_{3\pm} \in \mathbb{R}^3$ be the unit vectors defining the orientation of the periodic cell, and let $\boldsymbol{a}_1, \boldsymbol{a}_2, \boldsymbol{a}_3 \in \mathbb{R}^3$ define the rectangular unit cell such that $\boldsymbol{a}_3$ is coincident with the axis of rotation. (Note that this is not generally the same as the unit cell, nor is it unique for every choice of tilt axis.) The vectors defining the periodic cell used to represent each grain, shown in Fig. 2, are defined as $\{\lambda_i \boldsymbol{g}_{i\pm}\}$, which we express in terms of $\{\boldsymbol{a}_i\}$ as

$$\lambda_1\boldsymbol{g}_{1\pm} = m\,\boldsymbol{a}_1 \pm n\,\boldsymbol{a}_2, \qquad \lambda_2\boldsymbol{g}_{2\pm} = \mp p\,\boldsymbol{a}_1 + q\,\boldsymbol{a}_2, \quad (4)$$

where $m,n,p,q \in \mathbb{Z}$ are integral coefficients, and we note that $\boldsymbol{a}_3 = \boldsymbol{g}_3$ for tilt boundaries. The task at hand is to compute the integral coefficients given a tilt angle $\theta$. Generally, an arbitrary angle $\theta$ will be irrational (corresponding to periodically incommensurate boundaries), so it is necessary to locate the "closest" rational angle that defines an acceptably small periodic cell. This is done using the following equations, derived by an elementary geometric calculation:

$$(m,n) = \text{rat}_d\left[\frac{|\boldsymbol{a}_1|}{|\boldsymbol{a}_2|}\tan\theta\right], \qquad (p,q) = \text{rat}_d\left[\frac{|\boldsymbol{a}_2|}{|\boldsymbol{a}_1|}\tan\theta\right], \quad (5)$$

where $\text{rat}_d : \mathbb{R}\to\mathbb{Z}\times\mathbb{Z}$ is a rationalization function written in terms of a "maximum denominator" $d$, defined as

$$\text{rat}_d(\xi) = \underset{a,b\in\mathbb{Z},|a|\le d}{\arg\min} \left|\frac{b}{a} - \xi\right|. \quad (6)$$

That is, $d$ is an integer that determines the maximum allowable size of the periodic cell in terms of integer multiples of the original cell width. Increasing $d$ increases the density of data points in grain boundary space. The rational angle yielded using the formulae above is given by

$$\theta_{\text{rat}} = \tan^{-1}\left[\frac{n|\boldsymbol{a}_2|}{m|\boldsymbol{a}_1|}\right] \overset{!}{=} \tan^{-1}\left[\frac{p|\boldsymbol{a}_1|}{q|\boldsymbol{a}_2|}\right], \quad (7)$$

where $\overset{!}{=}$ denotes enforced equality. The enforced equality in Eq. (7) is critical because, especially for non-cubic periodic cells, rationalizations are not necessarily equal for both axes. The dimensions of the final unit cell used to construct the simulation domain are computed in terms of $m,n,p,q$, and $\theta_{\text{rat}}$ to be

$$\lambda_1 = m|\boldsymbol{a}_1|\cos\theta + n|\boldsymbol{a}_2|\sin\theta, \quad (8)$$

$$\lambda_2 = p|\boldsymbol{a}_1|\sin\theta + q|\boldsymbol{a}_2|\cos\theta, \quad (9)$$

where $\lambda_3 = 1$ for tilt boundaries. The $\Sigma$ value of the GB, a common classification used when describing tilt GBs, can be computed directly from these dimensions:

$$\Sigma = \min_{a\in\mathbb{Z}} \frac{1}{2^a}\,\text{int}\left[\frac{\lambda_1\lambda_2\lambda_3}{|\boldsymbol{a}_1\|\boldsymbol{a}_2\|\boldsymbol{a}_3|}\right] \quad \text{s.t.} \quad \text{int}\left[\frac{\lambda_1\lambda_2\lambda_3}{|\boldsymbol{a}_1\|\boldsymbol{a}_2\|\boldsymbol{a}_3|}\right] \bmod 2^a = 0. \quad (10)$$

This algorithm can readily be extended to other types of boundaries, but is used in its current form for the OpenKIM Test Driver we have written for this work. We emphasize that it allows the user to control the resolution of sampled boundaries in a tilt family by controlling only the maximum-denominator integer $d$. Conversely, given a maximum allowable repeating cell size, it can be used to generate a boundary configuration for an arbitrary tilt angle.

### 3.3. Estimation of ground state energy

It has been well-documented that GBs may exist in a large number of metastable configurations at 0K [44]. For a given IP, the particular configuration obtained depends on the initial guess and the energy minimization (optimization) method used. It is generally understood that these configurational parameters can substantially affect the result, making the ground state difficult to find [44]. Common practice [13,45] is to perform a high resolution grid search over available parameters, taking the lowest value. On the other hand, determination of the actual ground state demands computational resources well beyond those feasible for this high-throughput framework. Therefore, this Test Driver aims to strike an appropriate balance between management of computational resources and consistent, realistic test results across all

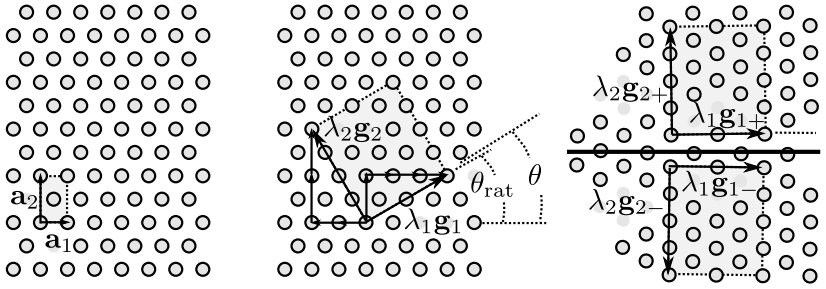


**Fig. 2.** For the set of FCC [111] tilt boundaries, given a value for $\theta$, we seek the nearest angle $\theta_{\text{rat}}$ so that a reasonably sized repeating cell can be constructed. The precise relative position of the two grains is determined by grid search, and overlapping atoms are deleted as described below.

platforms by performing a grid search with limited resolution. Such a grid search is not sufficiently fine to converge to the actual ground state. Instead, we aim for a search that is likely to report the energy of a representative, low-energy state that is neither the ground state, nor an artificially high energy state.

In the design of a grid search algorithmIn determining the ground state energy, there are usually two primary considerations: the atom deletion criterion and grain offsets. The first, atom deletion, is governed by a cutoff radius for eliminating atomic overlap. When generating initial configurations of GBs, the algorithm can create unphysical arrangements with one or more pairs of atoms located at identical or very close positions. In some cases, a consistent cutoff radius (for example, half the lattice constant) is used to eliminate atoms that are initially too close to each other [28]. However, this may result in undefined behavior for some IPs. As explained in Section 3, the approach used here is to set the cutoff to the lattice spacing at which the lattice energy exceeds the single-atom energy for the IP being used. This critical radius is determined for each IP based on values that are automatically referenced in the OpenKIM repository by the Test Driver.

The second consideration is the set of grain offsets used as initial guesses for energy minimization. The initial position of the top grain with respect to the bottom grain can substantially alter the energy, as reported in [41,43,46,47] and others. The standard approach is to perform a grid search over the space of initial translations: for each initial translation, allow the minimizer to find the local ground state, and then select the lowest of the returned results. High-resolution grid searches are often used when finding the ground state energy, but for efficiently estimating a representative metastable statecomputational tractability within this high-throughput system, the grid search in the OpenKIM Test Driver is limited to in-plane translations across the CSL, truncated according to symmetry, in increments of 1/4th of the relevant lattice constant.[2] Translations normal to the grain boundary are not explicitly considered. The number of translations considered, each of which requires a full energy minimization calculation, can range from 16 for a no-boundary case to thousands, depending on the misorientation. For each shift vector on the grid, the atomic positions and the dimensions of the orthogonal simulation box are relaxed in all directions, including the direction normal to the grain boundary, using the Polak–Ribière variant of the conjugate gradient method [48]. This implicitly explores translations of the grains normal to the grain boundary.

## 4. Computational results for symmetric tilt grain boundaries

In this section we present calculations for GB energies explored along the four inequivalent tilt axes that give rise to symmetric tilt boundaries in cubic materials [1]: [100], [110], [111], and [112]. This is far from an exhaustive study of all grain boundaries, but rather provides a representative sampling across a range of boundaries that demonstrates high angle and low angle cusp behavior. GB energy was calculated using the following Tests: fcc Al [428–431], fcc Cu [432–435], fcc Ni [436–439], fcc Fe, [440–443] bcc Fe, [444–447] and bcc Mo [448–451]. Iron is uniquely present for both fcc and bcc tests, where the only distinction between them is the initial condition of the lattice. For each chemical element, GB energies were computed for every matching potential in OpenKIM. The results presented herein are up-to-date as of December 2022, but the Tests are being continuously run and the latest results are available on openkim.org.

With such a large number of IPs fitted for different purposes, it is unavoidable that some of the computations result in errors or unphysical behavior. For example, a cause of several errors is that the OpenKIM Embedded Atom Model (EAM) Model Driver [29,162,452–454] raises an error when the electron density is outside of the fitted range of the embedding function, unlike other implementations of the EAM method that extrapolate. A full examination of every IP that caused errors and aberrant behavior is outside of the scope of the present work. However, some discussion of IP behavior is provided in Section 4.2. If an IP encountered errors for some tilt axes but not others, its energy curves are presented only on tilt axis plots corresponding to Tests for which no errors occurred.

### 4.1. General trends in grain boundary energy

Despite the diversity and complexity of GB energy calculations, the results are found to be remarkably well-behaved for the vast majority of the tested IPs. Included in this work is a series of plots illustrating the range of behaviors for the full spectrum of potentials currently available (as of December 2022) in OpenKIM for the aforementioned atomic species. To faithfully represent such a large number of energies in a compact way, we have ordered the IPs by their average energy across all GB tests. Therefore, the position of an IP in the legend is a rough indicator of its relative position in the spectrum, which may or may not be clearly visible due to the large number of potentials. Each IP in the legend contains its KIM ID (a shorthand designation indicating the potential type, authors, publication year, and supported chemical elements) and two or three citations: one is to the KIM Model (defining the IP parameters), one refers to the corresponding KIM Model Driver (containing the IP functional form, if applicable), and one is to the primary scientific source in which the IP was originally published. We encourage the reader to follow these citations to further investigate the behavior of IPs of interest and to directly access the data, which is published in the OpenKIM repository.

For the fcc metals, Al (Fig. 3), Cu (Fig. 4), Ni (Fig. 5), and Fe (Fig. 6), similar trends are noted and generally good behavior (i.e., stability of the boundary sufficient to calculate the relaxed GB formation energy) was observed. Remarkably, there is a variation of up to two or three fold in the average high angle GB energy calculated by different potentials; yet, the angles at which cusps in the energy occur are

[2] In some previous works [13,45] the lattice displacements were restricted to elements in the displacement-shift complete (DSC) lattice. We have opted instead to select offset vectors that are consistent between boundaries (i.e. irrespective of bicrystallography) in order to ensure consistent sampling of the ensemble of in-plane translations.

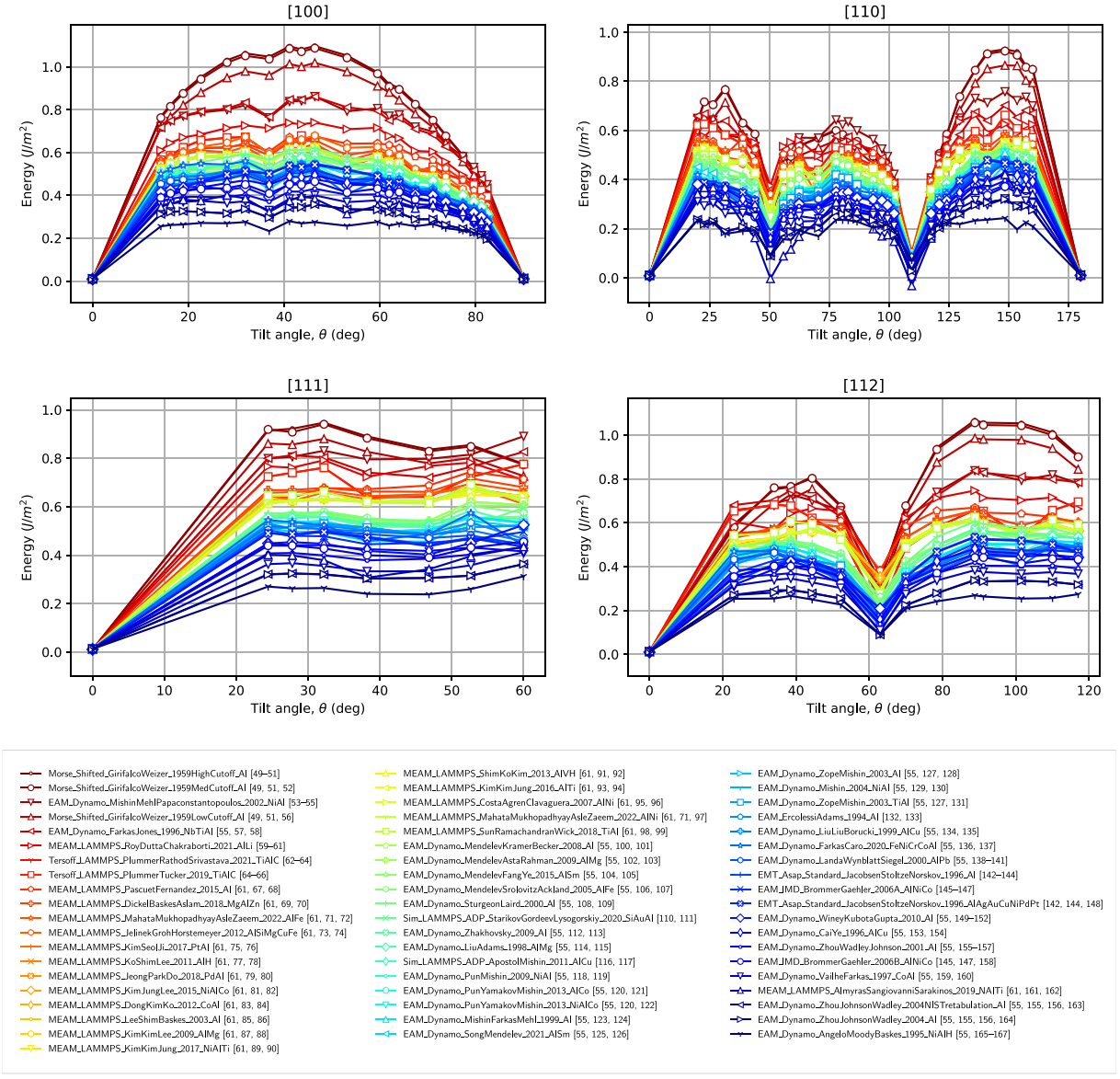


**Fig. 3.** GB energies for fcc Al [49–167].

consistent. For all fcc materials, especially, the $\Sigma 3$ boundary along the [110] axis exhibits close agreement across potentials. fcc Fe (Fig. 6) is the most disordered plot by far, with many potentials exhibiting unstable behavior. As the low-temperature ground state of iron is bcc, it is not surprising that many IPs rearrange the atoms so as to occupy this state.[3] Somewhat unexpectedly, however, many of the models are shown to be stable in the fcc phase for a large proportion of the GB configurations relevant to this work.

The GB energy relations computed for bcc Fe (Fig. 7) exhibit agreement amongst well-behaved potentials that rivals (and somewhat exceeds) that observed in the fcc metals. bcc Mo (Fig. 8) has the smallest spread among its well-behaved potentials, although this may simply be due to a lower number of tested potentials. The Morse pair potentials [66,326,367,454] exhibit unstable behavior for both bcc materials because pair potentials tend to favor close-packed structures such as fcc or hexagonal close-packed (hcp).[4] In the case of Mo, the pathological behavior of the Zhang and Nguyen Tersoff-style potential [29,138, 411,454] and the Stillinger–Weber (SW)-style MX2 potentials [403, 417,421] may be attributed to the fact that they are designed for two-dimensional multicomponent systems.

To further explore the question of energy variance between IPs, we consider the spectrum of microscopic degrees of freedom as a function of potential. Specifically, we consider six [110] tilt boundaries in fcc Al. Three of the configurations correspond to cusps in the energy ($\theta$ = 0°, 50.5°, 109.5°, Fig. 9(a)) and three to high-energy boundaries ($\theta$ = 20.1°, 77.8°, 124.1°, Fig. 9(b)). Even for this small selection, reporting the full selection of microstates for all ∼60 IPs is not feasible. Instead,

[3] Physically, the ground state of Fe is bcc up to ∼1180K. The fact that some potentials produce stable Fe fcc GBs at 0K does not necessarily reflect physical stability.

[4] We are aware of at least two methods used to stabilize pair potentials in the bcc structure. One is to use a double minimum in the energy curve. Another is to maintain a single minimum, but to use a cutoff that excludes the second nearest neighbor in fcc and design the curve such that the combined sum of first and second bcc neighbors is more stable than the sum of first fcc neighbors. The latter is used in the well-behaved modified Johnson (MJ) pair potential.

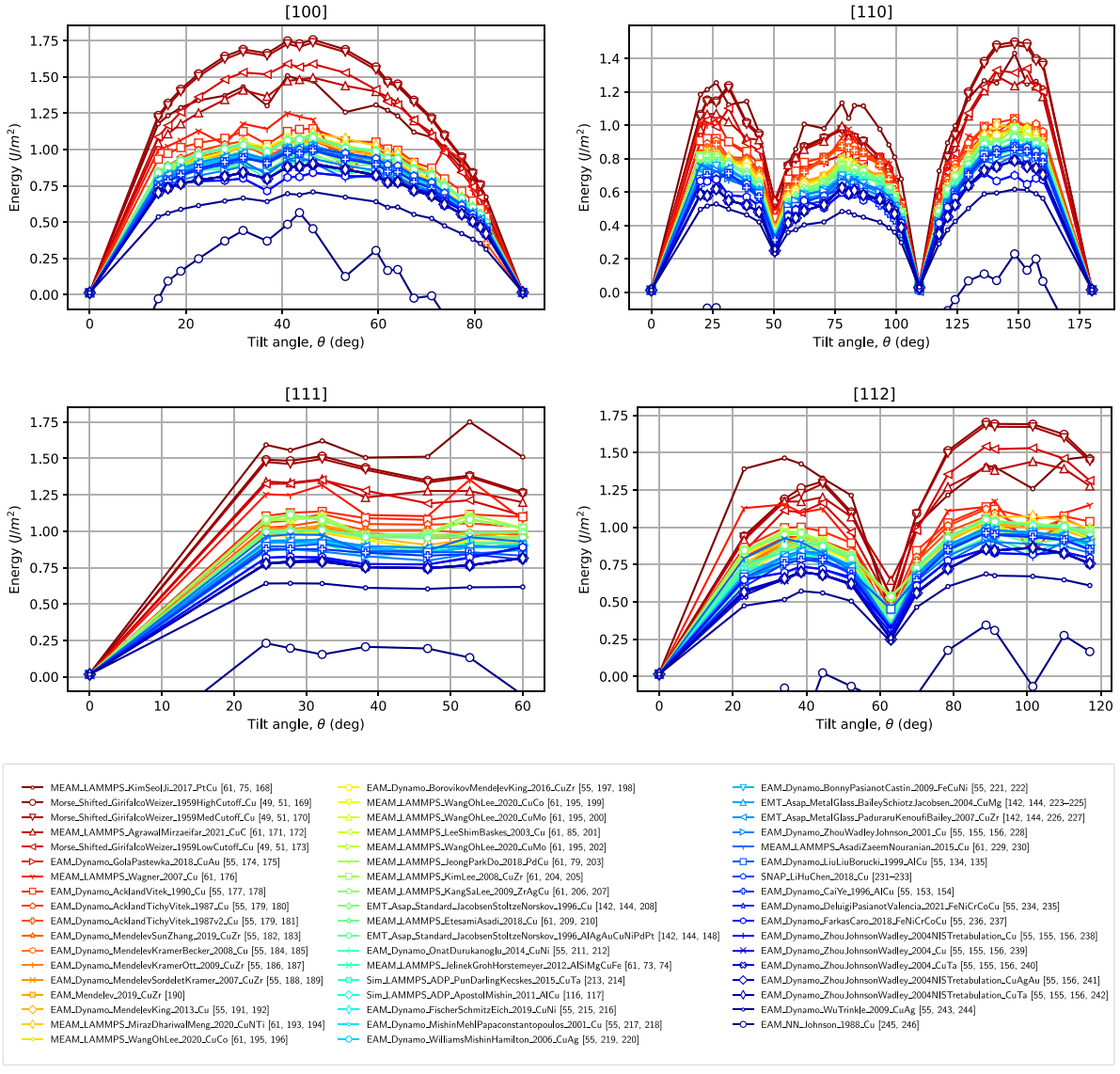


**Fig. 4.** GB energies for fcc Cu [51–53,57,66,72,88,94,110,120,122,123,126,131,133,136,140,154,156,162,168–246].

for each boundary, a histogram is presented showing the distribution of coordination numbers for each IP's lowest energy relaxed structure. The histograms of all Al IPs are superimposed, with the bars associated with a given IP colored to correspond to the legend color in Fig. 3. No differentiation is made between boundary atoms and non-boundary atoms, and so each histogram reflects the coordination numbers for all atoms in the simulation, including atoms in the bulk. This allows for a more straightforward comparison between IPs. However, it also means that the magnitude of the spike at #=12 depends on the normal simulation domain size, which varies from boundary to boundary. Therefore, while the histogram magnitudes may be compared potential-to-potential, they should not be compared boundary-to-boundary.

The $\theta = 0$ cusp corresponds to the absence of a GB. As expected, in this case all atoms have a coordination of 12, corresponding to the ideal fcc crystal structure. For the other two energy cusps, a scattering of additional coordinations appear in addition to 12. However, we note that there is a clear qualitative difference between these cusps. For the $\theta = 109.47°$ cusp, for most IPs, the ground state structure involves primarily three coordinations: 12, 9 and 6. This suggests that most of the IPs relax to a similar regular geometry, and indeed the scatter in energy at this cusp as seen in Fig. 3 for the [110] tilt axis is relatively small. In contrast, for the $\theta = 50.48°$ cusp, the spread in coordinations is broader and less uniform across IPs, suggesting a wider spread in structures, and indeed the spread in energy for this cusp is about 2.5 times larger than for $\theta = 109.47°$. This spread includes both IP effects (given the energy spread at $\theta = 0°$ for an identical structure), and configuration effects. Turning to the high-energy boundaries, we see that these exhibit a significantly larger spread in both coordination and energies (cf. Fig. 3), which indicates a broad spread in ground state structures. The spread in energy in this case is due both to the IP itself and the ground state structure (which depends indirectly on the IP), as also observed for the low-energy cusps.[5]

[5] Careful examination of Fig. 9 shows that there is not a direct relationship between configuration and energy across IPs. Were this true, it would be manifested in Fig. 9 as near-identical frequencies at each coordination number for any given energy band of IPs, e.g., all of the dark blue bands would have a similar frequency at any given coordination number for each subfigure. That is, the frequencies shown at a given coordination number in any subfigure would appear to vary (piecewise) continuously as the energy decreases from left to right. To the contrary, the rightmost column shows significant variance in coordination distribution for IPs that predict similar energies for the same GB. Hence, we conclude that different IPs may drive the minimizer to different

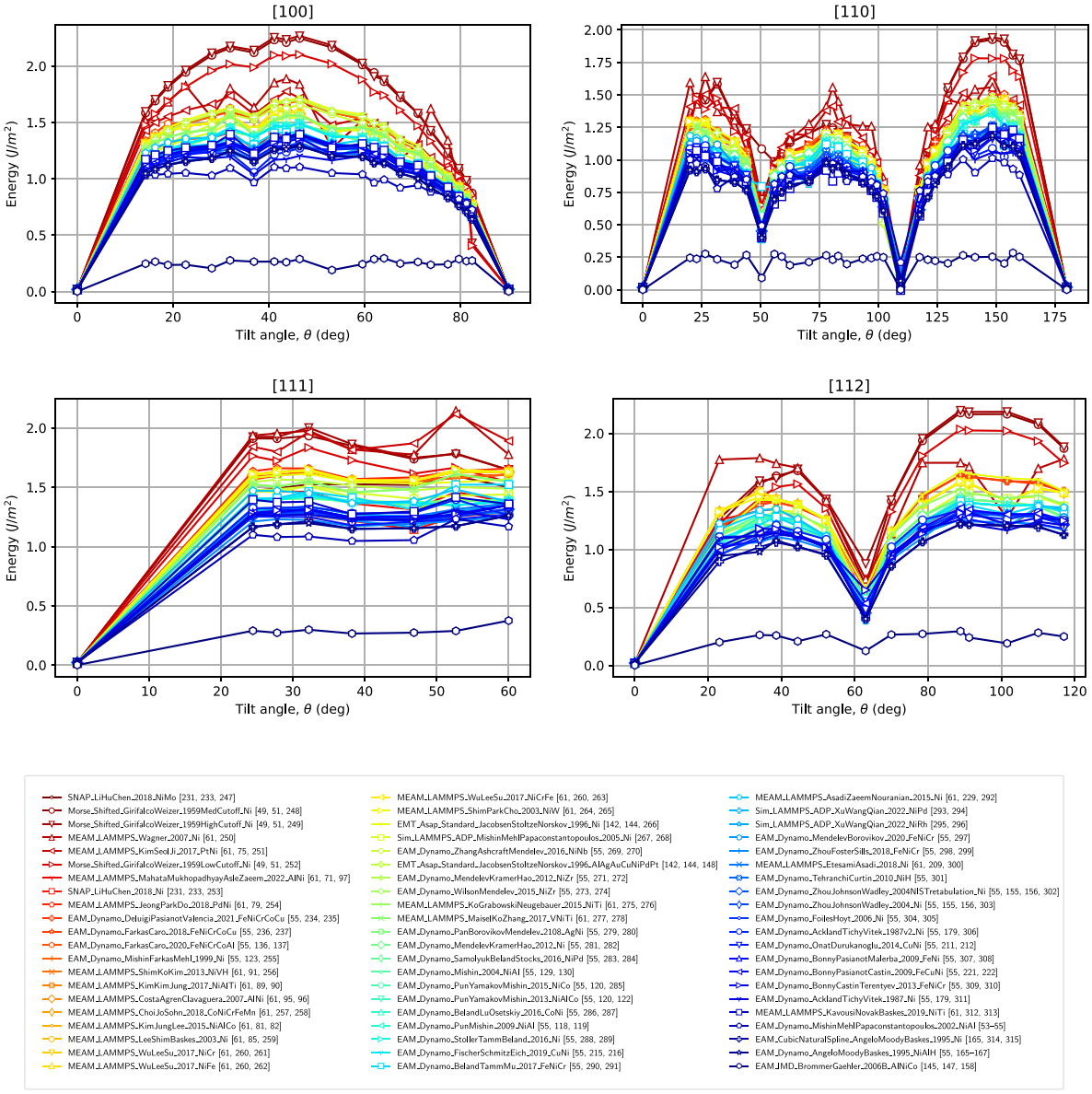


**Fig. 5.** GB energies for fcc Ni [51–53,55,57,58,60,63,64,66,68,69,72,77–79,82,87,94,98,111,115,119,120,124–126,128,131,133,137,148,152,158,162–164,166,170,171,176,179,184,194,198,205,208,210,217,218,223,225,238,247–315].

### 4.2. Examples of individual potential behavior

The data that has been presented may be used to compare IPs with respect to GB predictions, and to eventually design IPs to predict accurate boundary energies. Although an exhaustive analysis along these lines is outside the scope of this work, it is illuminating to examine the behavior of some specific IPs.

The GB energy tests produce for most IPs a ground state atomic structure that is well-behaved and has an expected form: the domain is divided into two symmetric grains separated in the center and across the periodic boundary by two well-defined GBs. For example, the result for bcc Fe for a 32° tilt about the [111] axis, run using the Zhou, Johnson, and Wadley EAM potential [390], is shown in Fig. 10a, and clearly has a well-behaved structure. Moreover, all of the potentials used in benchmark GB literature are well-behaved and produce roughly average results (with respect to the ensemble of IPs considered here). Of particular importance are the results for the two potentials used in the well-known Olmsted dataset [13] — the Foiles and Hoyt EAM potential [162,276] and the Ercolessi–Adams EAM potential [80,149]. Reasonable results and average energies are also found for the Mishin, Farkas, and Mehl EAM potential [87,162,315] used in Homer's recent work [45], as presented in Fig. 10b.

We now consider examples of IPs that produce unexpected results. The OpenKIM website provides easy access to descriptions of IPs, the original citation where the potential was developed, and selected comparisons of canonical properties (e.g., lattice and elastic constants). In the following examples, we demonstrate how such information can be used to explain the behavior of several IPs that were outliers, unstable, and/or failed to relax.

The EAM IMD potential of Schopf, Brommer, and Frigan for AlMnPd [58,457,458] was found to be unstable for fcc Al at high angle [110] boundaries. This is a potential developed for a complex metallic

configurations, but this does not fully explain the observed energy differences, one must also account for the differences between the IPs themselves.

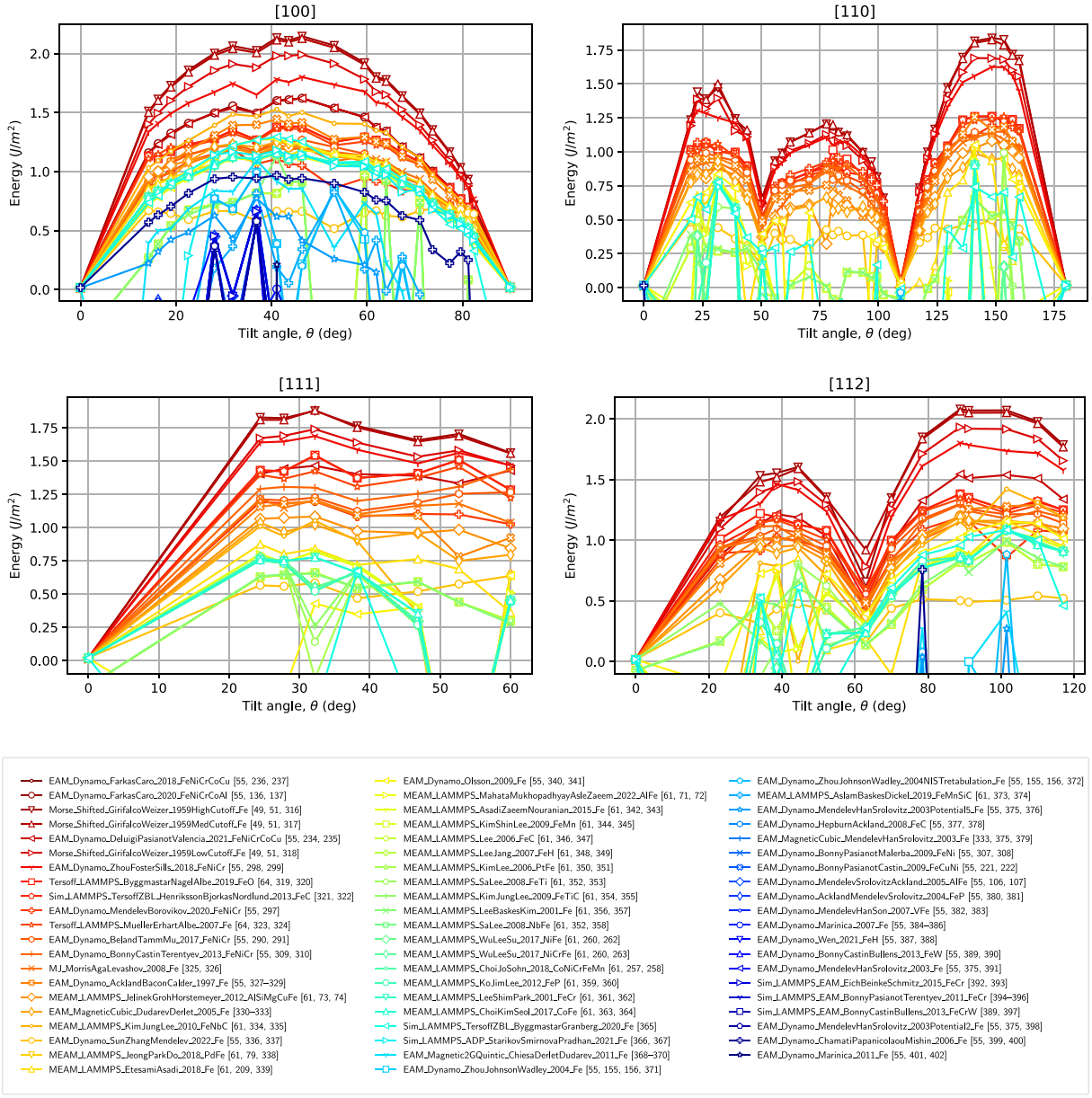


**Fig. 6.** GB energies for fcc Fe [52,57,66,69,72,73,77,83,88,119,126,131,138,140,141,162,170,179,194,198,205,208,238,250,252,254,256,262,277,279,288,290,295,300,304,309,314,316–402].

alloy (CMA) – the $\Xi$ phase of AlMnPd, which is a quasicrystal approximant. It is, therefore, not surprising that it does not provide an accurate description of fcc Al. Indeed, a further examination of the results of other Tests indicates that the corresponding lattice constant and elastic constants predicted by this IP are extreme in magnitude compared to the other potentials considered here and, furthermore, that its predicted ground state for pure Al is the hcp structure. Fig. 10c shows the relaxed configuration reached for a representative unstable fcc Al [110] boundary, where it can be seen that the initially fcc bulk has developed interspersed bands of atomic environments similar to those found in the hcp structure.

As mentioned in the previous section, the SW MX2 potential of Kurniawan, Petrie, and Williams [417] was developed for $MoS_2$ layers, and therefore is unsuitable for modeling bulk Mo. Indeed, there is a disclaimer on this potential's OpenKIM page stating as much, and its ground state can be seen to be hcp. Fig. 10d shows that at the angles where this potential exhibits unstable behavior, the pair of grain boundaries annihilates and the material relaxes to a nearly perfect hcp structure. The two EAM IMD potentials by Bromer and Gaehler ("A" [55,58,109] and "B" [55,58,64]) were developed for AlNiCo quasicrystals and both have extreme lattice and elastic constants for Ni. The "B" potential is an outlier for Ni, while the "A" potential had massively positive energies and numerous failures to relax, and is not included in the plots. On the other hand, the lattice and elastic constants for Al are less extreme for both potentials, and their GB energy relations for fcc Al exhibit unremarkable behavior. Finally, the EAM Dynamo potential of Sun, Zhang, and Mendelev for Fe [162,366,378] is an outlier for both fcc and bcc, although less so for fcc (Figs. 6 and 7). This potential is designed for high-pressure simulations of the Earth's core, and has extreme material constants.

In general, we found that the relaxed structures of energetically stable outliers were the same as those of well-behaved potentials. This should be expected based on their tendency to follow the trends of the energy-angle dependence, and only be incorrect in the magnitude of the GB energy.

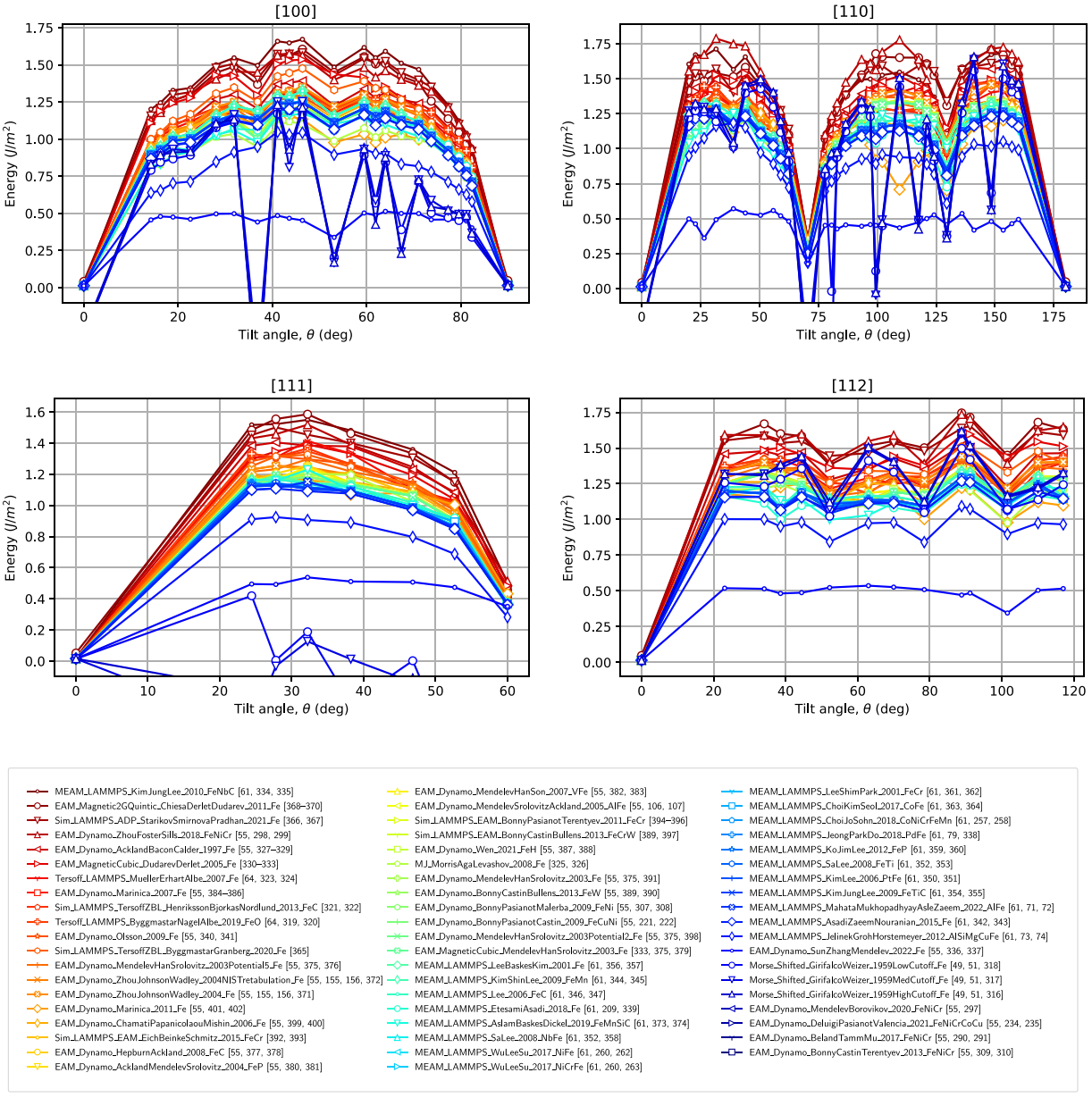


**Fig. 7.** GB energies for bcc Fe [52,57,66,72,73,83,88,119,126,131,138,140,141,162,170,179,198,208,238,250,252,254,256,262,277,279,288,290,295,300,304,309,314,316–382, 384–388,390–402].

### 4.3. Comparison to theoretical benchmark

Given the lack of experimental GB data for the full range of tilt boundaries, we use the results from a theoretical model for comparison. Combining the lattice matching model of [40] with the application of a facet-relaxation scheme [459] provides a benchmark for comparison that does not depend on an extensive set of fitting parameters. As a geometric/crystallographic method, the lattice matching model depends on only three parameters: (i) a window function parameter $\epsilon$ that correlates to cusp width, (ii) a thermalization parameter $\sigma$ that corresponds to temperature, and (iii) a scaling factor $E_0$. Determination of $\epsilon$ and $\sigma$ is relatively straightforward, and is discussed in great detail (along with a full presentation of the theory) in [460]. The parameter $E_0$, however, is a fitting parameter that linearly scales the reported energy. In prior work, it was found by calibration to existing atomistic data sets. These results indicate that there is considerable disagreement between potentials in what the correct value of $E_0$ may be.

An average over the potentials was taken and plotted alongside the lattice matching model fitted to that average for all available species (Figs. 11(a) and 11(b)). Although the IPs display a wide range of energy values, they also demonstrate a remarkable consistency in the general features of the GB energy landscape, correlating closely to the prediction of the geometric lattice matching energy model. This reinforces the hypothesis that GB energy is primarily driven by the geometry and crystallography, and is consistent across potentials and species up to a scaling factor. Yet, the value of the scaling factor itself remains undetermined, as the variance between models is large.

In light of the shortage of available experimental or ab initio data for validation, the large discrepancy in reported energy for different potentials causes some concern regarding the legitimacy of molecular dynamics GB energy calculations for any particular IP. Fig. 12 shows

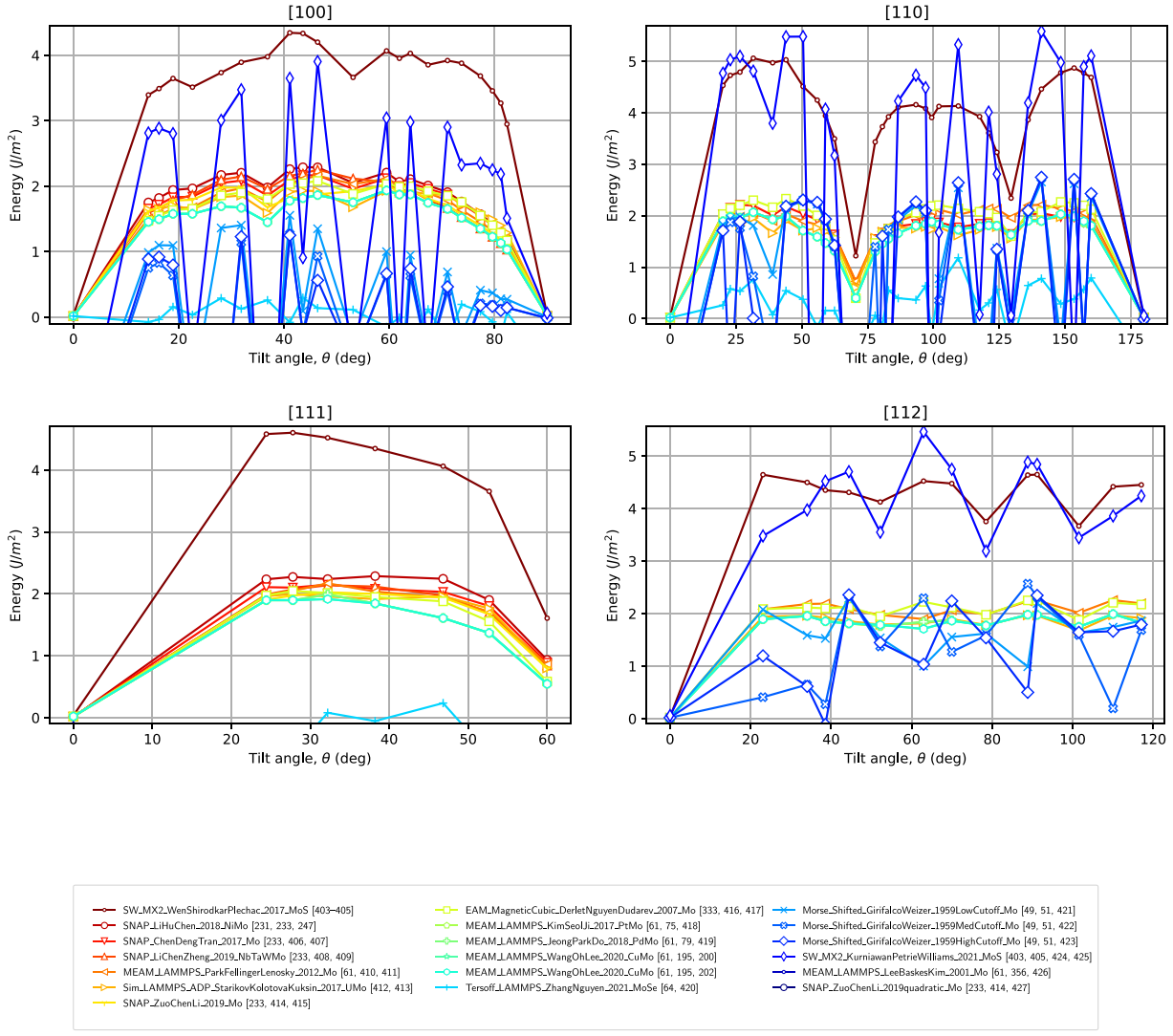


**Fig. 8.** GB energies for bcc Mo [52,53,57,66,131,138,210,211,216,218,232,308,350,382,403–427].

the distribution of average energies over the [110] tilt axes. In the case of Al potentials there appears to be some degree of agreement among many IPs with the distribution mostly concentrated near the mean, although this is not necessarily an indicator of accuracy. The distributions of fcc Cu and Ni are more lopsided, with the Fe and Mo series more erratic still. Overall, these results provide a sense of the uncertainty in GB energy predictions by classical IPs. The set of IPs that provide a prediction for a given GB comprise a *multi-model ensemble*. Studies in other physical domains, such as climate change [461], have shown that multi-model ensemble predictions generally outperform those of the "best" model, and are necessary to account for all aspects of model uncertainty (initial and boundary conditions, parametric and structural). However, care must be used when considering the prediction of a multi-model ensemble due to the possibilities for inter-model dependencies and biases, which can lead to double counting. For example, the high agreement between Al potentials may be due to the fact that many are EAM-type potentials that share a common structural bias and, in some cases, are not independent. Nevertheless the spread in IP predictions does provide an estimate of uncertainty. Future work should focus on methods for *weighting* ensemble members based on metrics for assessing their likely accuracy (e.g., by considering correlations between GB energy and other property predictions for which reference data is available), as done for example in the reliability ensemble average (REA) approach [462]. The OpenKIM framework is very amenable to such analysis, but a full exploration along these lines is left to future work.

### 4.4. Ongoing testing on OpenKIM.org

The framework presented here is accessible online, and the GB energy test result database is constantly updated as new potentials are added. The general and systematic framework used to generate these Tests makes it possible to add new Tests for more materials and IPs automatically. The current, raw data for the Tests presented here is available at https://openkim.org.

## 5. Conclusion

We have leveraged the OpenKIM framework to systematically compute atomistic symmetric tilt GB energies for multiple IPs and materials using a newly developed OpenKIM Test Driver. This system will continue to be applied to all future IPs that are uploaded to OpenKIM. The results from all simulations conducted as part of this study (as well as all future calculations) are available online at https://openkim.org, where they can be explored using text- and graphics-based visualization tools. The results of these calculations were compared and common trends identified, leading to the conclusion that although the overall

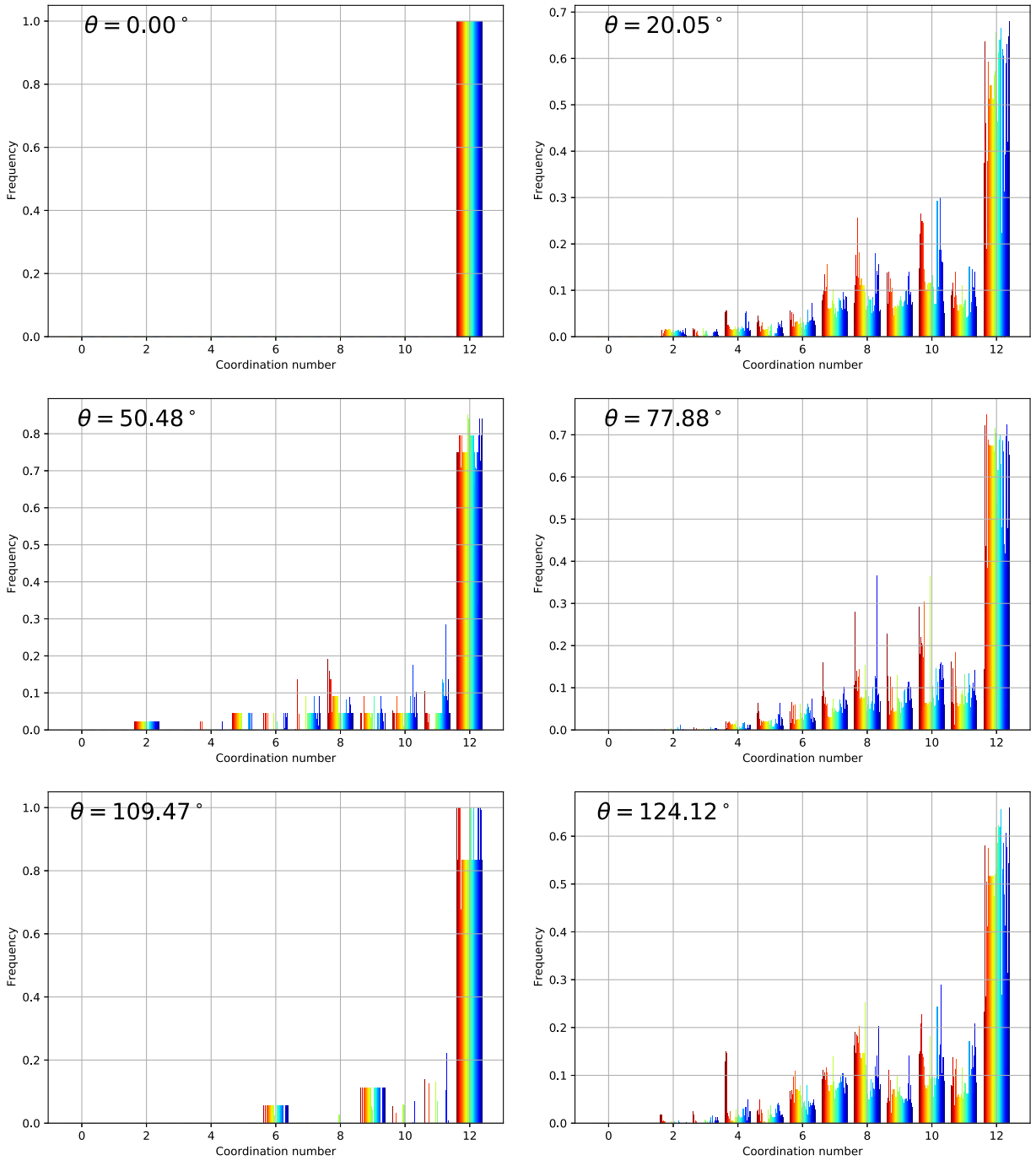


(a) Low-energy boundaries (cusps) (b) High-energy boundaries

**Fig. 9.** Combined counts of coordination numbers for all Al IPs at different angles of the [110] fcc Al boundary.

shape of the energy landscape appears to be IP-agnostic, the magnitude of the energy differs significantly between IPs and necessitates additional validation.

The foremost limitation of the results presented here is the relatively limited global optimization. Generally, determining the absolute ground state requires a high-resolution grid search over the microscopic GB degrees of freedom; here, only a relatively coarse search is performed due to the prohibitively excessive computational time required for a high-throughput framework. There are two reasons for this. First, the computational time required for a full resolution grid search is prohibitive for a high-throughput framework. Second, it is unlikely that ground states will be present in realistic calculations, especially when they are not reachable except by high-resolution grid search. Therefore, the energies found by the OpenKIM Test are more likely to be representative of actual energies in large simulations, and therefore of greater importance to most practitioners when simulating systems in which grain boundaries play a role.

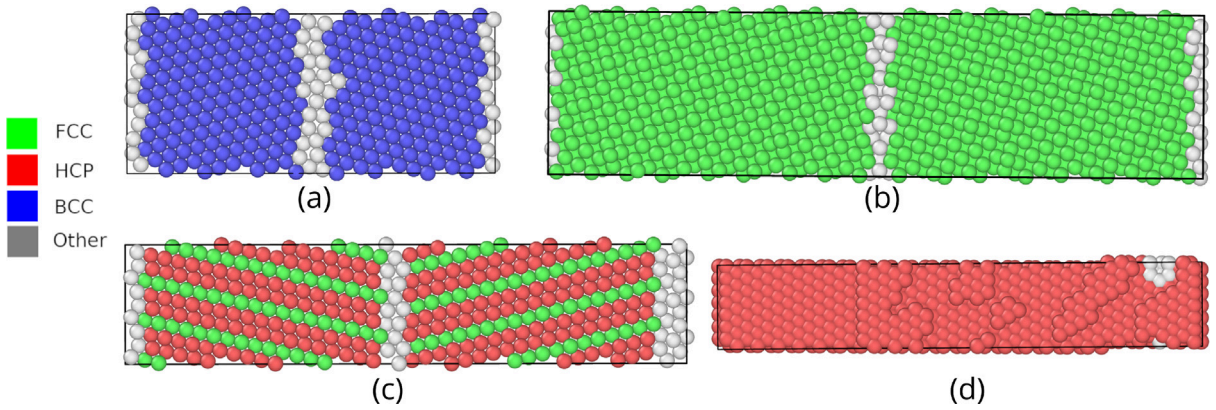


**Fig. 10.** Some notable post-relaxation GB configurations. Colors shown correspond to the local crystal structure as determined by the common neighbor analysis (CNA) [455] modifier in the OVITO visualization tool [456]. (a) shows a typical bcc Fe boundary using the EAM potential developed by Zhou, Johnson, and Wadley [390] tilted approximately 32 degrees about the [111] axis. (b) shows a typical fcc Al GB tilted approximately 31 degrees about the [100] axis using an EAM Dynamo potential by Mishin, Farkas, and Mehl [67]. (c) shows an unstable GB using an EAM IMD potential by Schopf, Brommer, and Frigan [457] that was initialized as fcc Al tilted 70 degrees about the [110] axis, but underwent a transition to an arrangement of alternating fcc and hcp layers. (d) shows what was initially a 55-degree GB about the [110] axis of bcc Mo using a Stillinger–Weber MX2 potential by Kurniawan, Petrie, and Williams [417], where the two grain boundaries required for periodic boundary conditions have annihilated and caused almost the entire configuration to transform into hcp.

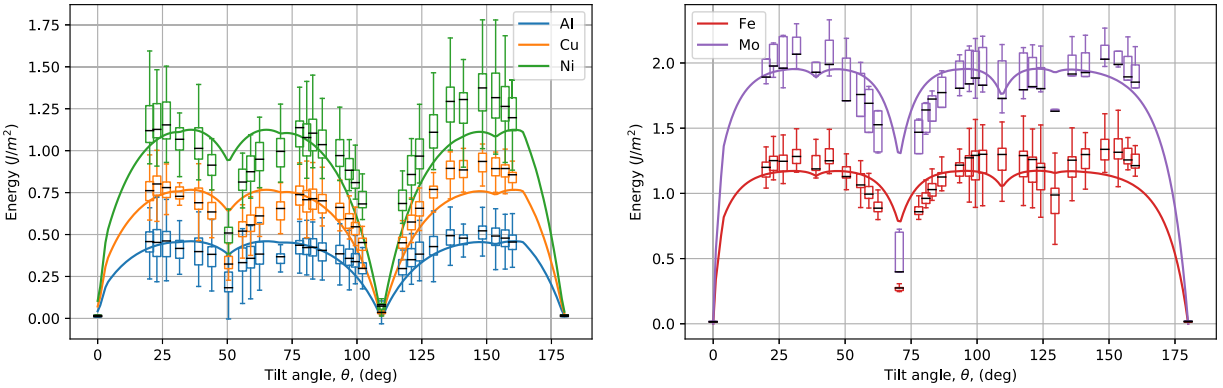


(a) fcc (b) bcc

**Fig. 11.** Statistical distribution of reported GB energy for all species and potentials over [1 1 0] tilt axes (box plots) compared to lattice matching (solid lines).

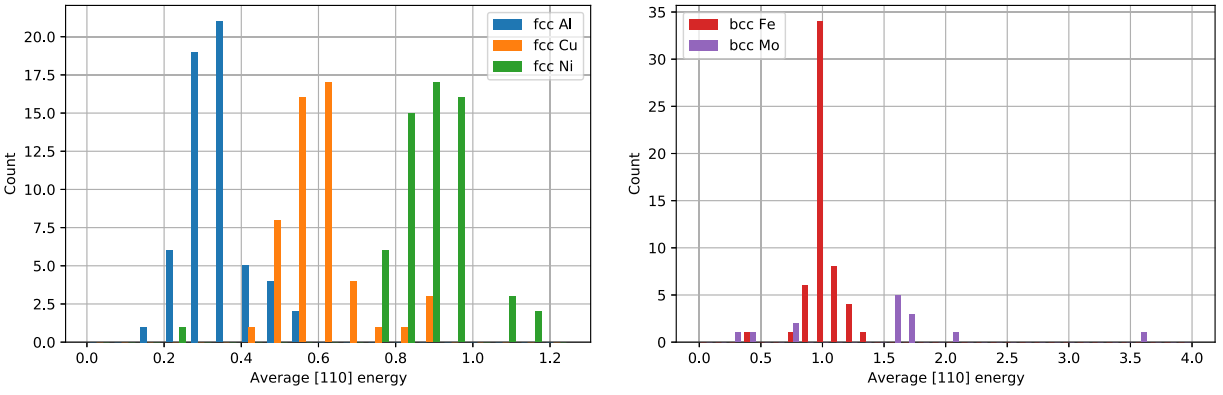


(a) (b)

**Fig. 12.** Distribution of energies averaged over [110] tilt axis for fcc tests (a) and bcc tests (b).

Future work will focus on extending this work to more general GBs and crystal structures, and to seeking connections between the predicted GB energy and other properties predicted by an IP in order to better assess the uncertainty in its GB energy predictions within a multi-model ensemble paradigm. To better approximate the ground state in future iterations of this KIM test, genetic methods such as the USPEX method [463,464] or the Monte Carlo method [465] may be used.

## CRediT authorship contribution statement

**Brendon Waters:** Software, Validation, Investigation, Writing – original draft, Writing – review & editing, Visualization. **Daniel S. Karls:** Methodology, Software, Validation, Investigation, Data curation, Writing – original draft, Writing – review & editing. **Ilia Nikiforov:** Investigation, Writing – original draft, Writing – review & editing. **Ryan S. Elliott:** Conceptualization, Software, Data curation, Supervision, Funding acquisition. **Ellad B. Tadmor:** Conceptualization, Software, Resources, Data curation, Writing – review & editing, Supervision, Funding acquisition. **Brandon Runnels:** Conceptualization, Methodology, Software, Formal analysis, Resources, Writing – original draft, Writing – review & editing, Visualization, Supervision, Funding acquisition.

## Declaration of competing interest

The authors declare the following financial interests/personal relationships which may be considered as potential competing interests: Brendon Waters reports financial support was provided by National Science Foundation. Daniel S. Karls reports financial support was provided by National Science Foundation. llia Nikiforov reports financial support was provided by National Science Foundation. Ryan S. Elliot reports financial support was provided by National Science Foundation. Ellad B. Tadmor reports financial support was provided by National Science Foundation. Brandon Runnels reports financial support was provided by National Science Foundation.

## Data availability

All data required to reproduce these findings are available to download from https://openkim.org/.

## Acknowledgments

The authors acknowledge partial support by the National Science Foundation, USA (NSF) under grants No. DMR-1834251, DMR-1834332, and OAC-1931304. BR acknowledges support from the National Science Foundation, USA, grant No. MOMS-2142164.

Computational support is acknowledged for the following resources: (1) Extreme Science and Engineering Discovery Environment (XSEDE) program allocation TG-PHY130007, which is supported by National Science Foundation, USA grant No. ACI-1053575 [466]; (2) Stampede2 supercomputer at the Texas Advanced Computing Center (TACC) as well as the Jetstream2 cloud computing environment at Indiana University through allocation MAT200008 from the Advanced Cyberinfrastructure Coordination Ecosystem: Services and Support (ACCESS) program, which is supported by National Science Foundation, USA grants No. 0941493; (3) Minnesota Supercomputing Institute (MSI) at the University of Minnesota; and (4) INCLINE cluster at the University of Colorado Colorado Springs, which is supported by the National Science Foundation, USA, grant No. OAC-2017917. The authors thank Mark Transtrum for helpful discussions.

## References

[1] A.P. Sutton, R.W. Balluffi, Interfaces in Crystalline Materials, Clarendon Press, 1995.
[2] P. Van Beers, G. McShane, V. Kouznetsova, M. Geers, Grain boundary interface mechanics in strain gradient crystal plasticity, J. Mech. Phys. Solids 61 (12) (2013) 2659–2679.
[3] I.J. Beyerlein, J. Wang, K. Kang, S.J. Zheng, N.A. Mara, Twinnability of bimetal interfaces in nanostructured composites, Mater. Res. Lett. 1 (2) (2013) 89–95.
[4] J.K. Chen, G. Chen, W.T. Reynolds, Interfacial structure and growth mechanisms of lath-shaped precipitates in Ni-45 wt% Cr, Phil. Mag. A 78 (2) (1998) 405–422.
[5] D. Brandon, B. Ralph, S.t. Ranganathan, M. Wald, A field ion microscope study of atomic configuration at grain boundaries, Acta Metall. 12 (7) (1964) 813–821.
[6] D. Smith, Can the CSL model fail? Scr. Metall. 14 (1980) 59–61.
[7] A.P. Sutton, E.P. Banks, A.R. Warwick, The five-dimensional parameter space of grain boundaries, Proc. R. Soc. Lond. Ser. A Math. Phys. Eng. Sci. 471 (2015) 20150442.
[8] T. Watanabe, S. Tsurekawa, The control of brittleness and development of desirable mechanical properties in polycrystalline systems by grain boundary engineering, Acta Mater. 47 (15) (1999) 4171–4185.
[9] W. Read, W. Shockley, Dislocation models of crystal grain boundaries, Phys. Rev. 78 (3) (1950) 275.
[10] F. Frank, The resultant content of dislocations in an arbitrary intercrystalline boundary, in: Symposium on the Plastic Deformation of Crystalline Solids, Vol. 150, 1950.
[11] W. Bollmann, Crystal Defects and Crystalline Interfaces, Springer Science & Business Media, 2012.
[12] V.V. Bulatov, B.W. Reed, M. Kumar, Grain boundary energy function for fcc metals, Acta Mater. 65 (2014) 161–175.
[13] D.L. Olmsted, S.M. Foiles, E.A. Holm, Survey of computed grain boundary properties in face-centered cubic metals: I. Grain boundary energy, Acta Mater. 57 (13) (2009) 3694–3703.
[14] D. Udler, D. Seidman, Grain boundary and surface energies of fcc metals, Phys. Rev. B 54 (16) (1996) R11133.
[15] T. Nishiyama, A. Seko, I. Tanaka, Application of machine learning potentials to predict grain boundary properties in fcc elemental metals, Phys. Rev. Mater. 4 (12) (2020) 123607.
[16] W. Ye, H. Zheng, C. Chen, S.P. Ong, A universal machine learning model for elemental grain boundary energies, Scr. Mater. 218 (2022) 114803.
[17] S. Patala, Understanding grain boundaries–The role of crystallography, structural descriptors and machine learning, Comput. Mater. Sci. 162 (2019) 281–294.
[18] B. Inkson, M. Mulvihill, G. Möbus, 3D determination of grain shape in a FeAl-based nanocomposite by 3D FIB tomography, Scr. Mater. 45 (7) (2001) 753–758.
[19] P. Midgley, M. Weyland, 3D electron microscopy in the physical sciences: the development of Z-contrast and EFTEM tomography, Ultramicroscopy 96 (3) (2003) 413–431.
[20] N.A. Gjostein, F. Rhines, Absolute interfacial energies of [001] tilt and twist grain boundaries in copper, Acta Metall. 7 (5) (1959) 319–330.
[21] H. Miura, M. Kato, T. Mori, Temperature dependence of the energy of Cu [110] symmetrical tilt grain boundaries, J. Mater. Sci. Lett. 13 (1) (1994) 46–48.
[22] D. Wolf, Structure-energy correlation for grain boundaries in FCC metals–I. Boundaries on the (111) and (100) planes, Acta Metall. 37 (7) (1989) 1983–1993.
[23] D. Wolf, Structure-energy correlation for grain boundaries in fcc metals–II. Boundaries on the (110) and (113) planes, Acta Metall. 37 (10) (1989) 2823–2833.
[24] D. Wolf, Structure-energy correlation for grain boundaries in FCC metals–III. Symmetrical tilt boundaries, Acta Metall. Mater. 38 (5) (1990) 781–790.
[25] D. Wolf, Structure-energy correlation for grain boundaries in fcc metals–IV. Asymmetrical twist (general) boundaries, Acta Metall. Mater. 38 (5) (1990) 791–798.
[26] D. Wolf, Correlation between the energy and structure of grain boundaries in bcc metals I. Symmetrical boundaries on the (110) and (100) planes, Phil. Mag. B 59 (6) (1989) 667–680.
[27] D. Wolf, Correlation between the energy and structure of grain boundaries in bcc metals. II. Symmetrical tilt boundaries, Phil. Mag. A 62 (4) (1990) 447–464.
[28] E.N. Hahn, S.J. Fensin, T.C. Germann, M.A. Meyers, Symmetric tilt boundaries in body-centered cubic tantalum, Scr. Mater. 116 (2016) 108–111.
[29] E.B. Tadmor, R.S. Elliott, J.P. Sethna, R.E. Miller, C.A. Becker, The potential of atomistic simulations and the knowledgebase of interatomic models, JOM 63 (7) (2011) 17.
[30] E.B. Tadmor, R.S. Elliott, S.R. Phillpot, S.B. Sinnott, NSF cyberinfrastructures: A new paradigm for advancing materials simulation, Curr. Opin. Solid State Mater. Sci. 17 (6) (2013) 298–304.
[31] R.S. Elliott, E.B. Tadmor, KIM Application Programming Interface (API) standard, 2016, https://openkim.org/kim-api/.
[32] D. Karls, M. Bierbaum, A. Alemi, R. Elliott, J. Sethna, E. Tadmor, The OpenKIM processing pipeline: A cloud-based automatic material property computation engine, J. Chem. Phys. 153 (6) (2020) 064104.
[33] D.S. Karls, S.M. Clark, B.A. Waters, R.S. Elliott, E.B. Tadmor, HPC extensions to the OpenKIM processing pipeline, in: 2022 IEEE 18th International Conference on e-Science (e-Science), 2022, pp. 278–283.
[34] OpenKIM query language, 2016, https://query.openkim.org.
[35] A.P. Thompson, H.M. Aktulga, R. Berger, D.S. Bolintineanu, W.M. Brown, P.S. Crozier, P.J. in 't Veld, A. Kohlmeyer, S.G. Moore, T.D. Nguyen, R. Shan, M.J. Stevens, J. Tranchida, C. Trott, S.J. Plimpton, LAMMPS - a flexible simulation tool for particle-based materials modeling at the atomic, meso, and continuum scales, Comput. Phys. Comm. 271 (2022) 108171.
[36] B. Runnels, D.S. Karls, B. Waters, Relaxed energy as a function of tilt angle for a symmetric tilt grain boundary within a cubic crystal v003, 2022, http://dx.doi.org/10.25950/2c59c9d6, OpenKIM.

[37] J.W. Gibbs, H.A. Bumstead, W.R. Longley, et al., The Collected Works of J. Willard Gibbs, Vol. 1, Longmans, Green and Company, 1928.
[38] A. Arya, E.A. Carter, Structure, bonding, and adhesion at the TiC (100)/Fe (110) interface from first principles, J. Chem. Phys. 118 (19) (2003) 8982–8996.
[39] D. Jiang, E.A. Carter, Prediction of strong adhesion at the MoSi 2/Fe interface, Acta Mater. 53 (17) (2005) 4489–4496.
[40] B. Runnels, I.J. Beyerlein, S. Conti, M. Ortiz, An analytical model of interfacial energy based on a lattice-matching interatomic energy, J. Mech. Phys. Solids 89 (2016) 174–193.
[41] M. Tschopp, G. Tucker, D. McDowell, Structure and free volume of <110> symmetric tilt grain boundaries with the E structural unit, Acta Mater. 55 (11) (2007) 3959–3969.
[42] M. Tschopp, G. Tucker, D. McDowell, Atomistic simulations of tension–compression asymmetry in dislocation nucleation for copper grain boundaries, Comput. Mater. Sci. 44 (2) (2008) 351–362.
[43] M. Tschopp, D. McDowell, Asymmetric tilt grain boundary structure and energy in copper and aluminium, Phil. Mag. 87 (25) (2007) 3871–3892.
[44] J. Han, V. Vitek, D.J. Srolovitz, Grain-boundary metastability and its statistical properties, Acta Mater. 104 (2016) 259–273.
[45] E.R. Homer, G.L. Hart, C. Braxton Owens, D.M. Hensley, J.C. Spendlove, L.H. Serafin, Examination of computed aluminum grain boundary structures and energies that span the 5D space of crystallographic character, Acta Mater. 234 (2022) 118006.
[46] M. Tschopp, D. McDowell, Structures and energies of $\sigma$ 3 asymmetric tilt grain boundaries in copper and aluminium, Phil. Mag. 87 (22) (2007) 3147–3173.
[47] G.J. Tucker, M.A. Tschopp, D.L. McDowell, Evolution of structure and free volume in symmetric tilt grain boundaries during dislocation nucleation, Acta Mater. 58 (19) (2010) 6464–6473.
[48] E. Polak, Optimization: Algorithms and Consistent Approximations, Vol. 124, Springer Science & Business Media, 2012.
[49] J.-H. Shim, W.-S. Ko, K.-H. Kim, H.-S. Lee, Y.-S. Lee, J.-Y. Suh, Y.W. Cho, B.-J. Lee, MEAM Potential for the Al-V-H system developed by Shim et al. (2013) v001, 2021, http://dx.doi.org/10.25950/7d83c8c4, OpenKIM.
[50] B.-J. Lee, J.-H. Shim, M.I. Baskes, MEAM Potential for Al developed by Lee, Shim, and Baskes (2003) v000, 2022, http://dx.doi.org/10.25950/48eea824, OpenKIM.
[51] K. Jacobsen, P. Stoltze, J. Nørskov, A semi-empirical effective medium theory for metals and alloys, Surf. Sci. 366 (2) (1996) 394–402.
[52] L.A. Girifalco, V.G. Weizer, Application of the Morse potential function to cubic metals, Phys. Rev. 114 (3) (1959) 687.
[53] J.-S. Kim, D. Seol, J. Ji, H.-S. Jang, Y. Kim, B.-J. Lee, Second nearest-neighbor modified embedded-atom method interatomic potentials for the Pt-M (M=Al, Co, Cu, Mo, Ni, Ti, V) binary systems, CALPHAD 59 (2017) 131–141.
[54] Y.-M. Kim, N.J. Kim, B.-J. Lee, MEAM Potential for the Al-Mg system developed by Kim, Kim, and Lee (2009) v001, 2021, http://dx.doi.org/10.25950/46bc576f, OpenKIM.
[55] P. Brommer, F. Gähler, Effective potentials for quasicrystals from ab-initio data, Phil. Mag. 86 (6–8) (2006) 753–758.
[56] S. Roy, A. Dutta, N. Chakraborti, MEAM potential for Al and Al-Li alloys developed by Roy, Dutta, and Chakraborti (2021) v000, 2021, http://dx.doi.org/10.25950/96965eb6, OpenKIM.
[57] Y. Afshar, S. Hütter, R.E. Rudd, A. Stukowski, W.W. Tipton, D.R. Trinkle, G.J. Wagner, P. Zhang, E. Alonso, M.I. Baskes, V.V. Bulatov, T.D. de la Rubia, J. Kim, J.D. Kress, B.-J. Lee, T. Lenosky, J.S. Nelson, B. Sadigh, A.F. Voter, A.F. Wright, Modified embedded atom method (MEAM) Model Driver v001, 2021, http://dx.doi.org/10.25950/773efb8e, OpenKIM.
[58] D. Schopf, EAM implementation from the IMD code v003, 2018, http://dx.doi.org/10.25950/e28996e9, OpenKIM.
[59] D. Farkas, EAM potential (LAMMPS cubic hermite tabulation) for the Co-Al system developed by Vailhe and Farkas (1997) v005, 2018, http://dx.doi.org/10.25950/32f48dd4, OpenKIM.
[60] A.C. e Silva, J. Ågren, M.T. Clavaguera-Mora, D. Djurovic, T. Gomez-Acebo, B.-J. Lee, Z.-K. Liu, P. Miodownik, H.J. Seifert, Applications of computational thermodynamics-the extension from phase equilibrium to phase transformations and other properties, CALPHAD 31 (1) (2007) 53–74.
[61] M.I. Pascuet, J.R. Fernández, MEAM potential for Al developed by Pascuet and Fernandez (2015) v001, 2021, http://dx.doi.org/10.25950/cf7fcbd4, OpenKIM.
[62] M. Mendelev, M. Kramer, C. Becker, M. Asta, Analysis of semi-empirical interatomic potentials appropriate for simulation of crystalline and liquid Al and Cu, Phil. Mag. 88 (12) (2008) 1723–1750.
[63] Y.-K. Kim, H.-K. Kim, W.-S. Jung, B.-J. Lee, Development and application of Ni-Ti and Ni-Al-Ti 2NN-MEAM interatomic potentials for Ni-base superalloys, Comput. Mater. Sci. 139 (2017) 225–233.
[64] D. Schopf, EAM potential (IMD tabulation) for the Al-Ni-Co system for quasicrystals developed by Brommer and Gaehler (2006); Potential B v003, 2018, http://dx.doi.org/10.25950/a978894d, OpenKIM.
[65] J.M. Winey, A. Kubota, Y.M. Gupta, A thermodynamic approach to determine accurate potentials for molecular dynamics simulations: thermoelastic response of aluminum, Modelling Simul. Mater. Sci. Eng. 17 (5) (2009) 055004.
[66] R.S. Elliott, Y. Afshar, Morse pair potential shifted to zero energy at cutoff separation v004, 2020, http://dx.doi.org/10.25950/dd56cab5, OpenKIM.
[67] Y. Mishin, EAM potential (LAMMPS cubic hermite tabulation) for Al developed by Mishin et al. (1999) v005, 2018, http://dx.doi.org/10.25950/dbe54c2e, OpenKIM.
[68] Y.-K. Kim, W.-S. Jung, B.-J. Lee, MEAM Potential for the Ni-Al-Co system developed by Kim, Jung, and Lee, (2015) v001, 2021, http://dx.doi.org/10.25950/48cbcad3, OpenKIM.
[69] D. Farkas, A. Caro, EAM potential (LAMMPS cubic hermite tabulation) for the Fe-Ni-Cr-Co-Al system developed by Farkas and Caro (2020) v000, 2022, http://dx.doi.org/10.25950/8c495c7e, OpenKIM.
[70] R.S. Elliott, Morse potential (shifted) for Al by Girifalco and Weizer (1959) using a low-accuracy cutoff distance v004, 2020, http://dx.doi.org/10.25950/977dc2ac, OpenKIM.
[71] A. Landa, P. Wynblatt, E. Johnson, U. Dahmen, Computer simulation of Pb/Al interfaces, Acta Mater. 48 (10) (2000) 2557–2563.
[72] X. Zhou, H. Wadley, R.A. Johnson, D. Larson, N. Tabat, A. Cerezo, A. Petford-Long, G. Smith, P. Clifton, R. Martens, et al., Atomic scale structure of sputtered metal multilayers, Acta Mater. 49 (19) (2001) 4005–4015.
[73] A. Mahata, T. Mukhopadhyay, M.A. Zaeem, MEAM Potential for the Al-Fe system developed by Mahata, Mukhopadhyay and Asle Zaeem (2022) v000, 2022, http://dx.doi.org/10.25950/359f6927, OpenKIM.
[74] E. Tadmor, EAM potential (LAMMPS cubic hermite tabulation) for the Al-Mg system developed by Liu and Adams (1998) v000, 2018, http://dx.doi.org/10.25950/3f4d32ac, OpenKIM.
[75] D. Farkas, C. Jones, Interatomic potentials for ternary Nb-Ti-Al alloys, Modelling Simul. Mater. Sci. Eng. 4 (1) (1996) 23.
[76] J.M. Winey, A. Kubota, Y.M. Gupta, Thermodynamic approach to determine accurate potentials for molecular dynamics simulations: thermoelastic response of aluminum, Modelling Simul. Mater. Sci. Eng. 18 (2) (2010) 029801.
[77] D. Farkas, A. Caro, Model interatomic potentials for Fe–Ni–Cr–Co–Al high-entropy alloys, J. Mater. Res. 35 (22) (2020) 3031–3040.
[78] Y. Mishin, EAM potential (LAMMPS cubic hermite tabulation) for the Ni-Al system developed by Purja Pun and Minshin (2009) v005, 2018, http://dx.doi.org/10.25950/3c5eec8c, OpenKIM.
[79] G.P.P. Pun, Y. Mishin, Development of an interatomic potential for the Ni-Al system, Phil. Mag. 89 (34–36) (2009) 3245–3267.
[80] F. Ercolessi, J.B. Adams, Interatomic potentials from first-principles calculations: The force-matching method, Europhys. Lett. 26 (8) (1994) 583.
[81] Y.-M. Kim, N.J. Kim, B.-J. Lee, Atomistic modeling of pure Mg and Mg–Al systems, CALPHAD 33 (4) (2009) 650–657.
[82] Y.-K. Kim, W.-S. Jung, B.-J. Lee, Modified embedded-atom method interatomic potentials for the Ni–Co binary and the Ni–Al–Co ternary systems, Modelling Simul. Mater. Sci. Eng. 23 (5) (2015) 055004.
[83] M.I. Mendelev, Finnis–Sinclair potential (LAMMPS cubic hermite tabulation) for the Al-Fe system developed by Mendelev et al. (2005) v005, 2018, http://dx.doi.org/10.25950/448f3c57, OpenKIM.
[84] E. Tadmor, EAM potential (LAMMPS cubic hermite tabulation) for the Nb-Ti-Al system developed by Farkas and Jones (1996) v000, 2018, http://dx.doi.org/10.25950/3eacab42, OpenKIM.
[85] S. Starikov, I. Gordeev, Y. Lysogorskiy, L. Kolotova, S. Makarov, Optimized interatomic potential for study of structure and phase transitions in Si-Au and Si-Al system, Comput. Mater. Sci. 184 (2020) 109891.
[86] J.A. Zimmerman, EAM potential (LAMMPS cubic hermite tabulation) for Al for shock compression at room and higher temperatures developed by Winey, Kubota and Gupta (2010) v005, 2018, http://dx.doi.org/10.25950/23542694, OpenKIM.
[87] Y. Mishin, D. Farkas, M. Mehl, D. Papaconstantopoulos, Interatomic potentials for monoatomic metals from experimental data and ab initio calculations, Phys. Rev. B 59 (5) (1999) 3393.
[88] B. Jelinek, S. Groh, M.F. Horstemeyer, J. Houze, S.G. Kim, G.J. Wagner, A. Moitra, M.I. Baskes, Modified embedded atom method potential for Al, Si, Mg, Cu, and Fe alloys, Phys. Rev. B 85 (2012) 245102.
[89] S. Roy, A. Dutta, N. Chakraborti, A novel method of determining interatomic potential for Al and Al-Li alloys and studying strength of Al-Al3Li interphase using evolutionary algorithms, Comput. Mater. Sci. 190 (2021) 110258.
[90] M.I. Mendelev, Finnis–Sinclair potential (LAMMPS cubic hermite tabulation) for solid-liquid interfaces in Al-Mg alloys developed by Mendelev et al. (2009) v005, 2018, http://dx.doi.org/10.25950/fbec42d2, OpenKIM.
[91] G. Plummer, H. Rathod, A. Srivastava, M. Radovic, T. Ouisse, M. Yildizhan, P. Persson, K. Lambrinou, M. Barsoum, G. Tucker, On the origin of kinking in layered crystalline solids, Mater. Today 43 (2021) 45–52.
[92] J. Schiotz, EMT potential for Al developed by Jacobsen, Stoltze, and Norskov (1996) v001, 2019, http://dx.doi.org/10.25950/bdbaee6a, OpenKIM.
[93] Y. Mishin, EAM potential (LAMMPS cubic hermite tabulation) for the Ti–Al system developed by Zope and Mishin (2003) v000, 2018, http://dx.doi.org/10.25950/d3553497, OpenKIM.
[94] J. Schiotz, EMT potential for Al, Ni, Cu, Pd, Ag, Pt and Au developed by Jacobsen, Stoltze, and Norskov (1996) v001, 2019, http://dx.doi.org/10.25950/485ab326, OpenKIM.
[95] S. Starikov, LAMMPS ADP potential for the Si-Au-Al system developed by Starikov et al. (2020) v000, 2020, http://dx.doi.org/10.25950/4e5bdc47, OpenKIM.

[96] G. Plummer, G.J. Tucker, Bond-order potentials for the $Ti_3AlC_2$ and $Ti_3SiC_2$ MAX phases, Phys. Rev. B 100 (2019) 214114.
[97] M.I. Mendelev, Finnis–Sinclair potential (LAMMPS cubic hermite tabulation) for Al developed by Mendelev et al. (2008) v005, 2018, http://dx.doi.org/10.25950/c7946b4e, OpenKIM.
[98] Y.-K. Kim, H.-K. Kim, W.-S. Jung, B.-J. Lee, MEAM Potential for the Ni-Al-Ti system developed by Kim et al. (2017) v001, 2021, http://dx.doi.org/10.25950/c22b937c, OpenKIM.
[99] Y.-K. Kim, H.-K. Kim, W.-S. Jung, B.-J. Lee, MEAM Potential for the Al-Ti system developed by Kim et al. (2016) v001, 2021, http://dx.doi.org/10.25950/5e42e934, OpenKIM.
[100] E. Tadmor, Finnis–Sinclair potential (LAMMPS cubic hermite tabulation) for the Al-Sm system developed by Mendelev et al. (2015) v000, 2018, http://dx.doi.org/10.25950/2ef556c6, OpenKIM.
[101] G. Plummer, G.J. Tucker, Tersoff-style three-body potential for TiAlC developed by Plummer and Tucker (2019) v000, 2022, http://dx.doi.org/10.25950/3cac382d, OpenKIM.
[102] E. Tadmor, EAM potential (LAMMPS cubic hermite tabulation) for Al developed by Zhou, Wadley and Johnson (2001) v000, 2018, http://dx.doi.org/10.25950/84f935c7, OpenKIM.
[103] R.S. Elliott, EAM potential (LAMMPS cubic hermite tabulation) for Al optimized for melting temperature developed by Sturgeon and Laird (2000) v005, 2018, http://dx.doi.org/10.25950/d62edb43, OpenKIM.
[104] M.I. Mendelev, F. Zhang, Z. Ye, Y. Sun, M.C. Nguyen, S.R. Wilson, C.Z. Wang, K.M. Ho, Development of interatomic potentials appropriate for simulation of devitrification of Al 90 Sm 10 alloy, Modelling Simul. Mater. Sci. Eng. 23 (4) (2015) 045013.
[105] H. Song, M.I. Mendelev, EAM potential (LAMMPS cubic hermite tabulation) for the Al-Sm system developed by Song and Mendelev (2021) v000, 2022, http://dx.doi.org/10.25950/3c993b22, OpenKIM.
[106] G.-U. Jeong, C.S. Park, H.-S. Do, S.-M. Park, S. Lee, MEAM Potential for the Pd-Al system developed by Jeong et al. (2018) v001, 2021, http://dx.doi.org/10.25950/eedebe23, OpenKIM.
[107] J.-S. Kim, D. Seol, J. Ji, H.-S. Jang, B.-J. Lee, MEAM Potential for the Pt-Al system developed by Kim and Lee (2017) v001, 2021, http://dx.doi.org/10.25950/63fc3383, OpenKIM.
[108] C. Vailhé, D. Farkas, Shear faults and dislocation core structures in B2 CoAl, J. Mater. Res. 12 (10) (1997) 2559–2570.
[109] D. Schopf, EAM potential (IMD tabulation) for the Al-Ni-Co system for quasicrystals developed by Brommer and Gaehler (2006); Potential A v003, 2018, http://dx.doi.org/10.25950/ad45aa37, OpenKIM.
[110] E. Tadmor, EAM potential (LAMMPS cubic hermite tabulation) for the Al-Cu system developed by Liu et al. (1999) v000, 2018, http://dx.doi.org/10.25950/2dd77629, OpenKIM.
[111] M.I. Baskes, X. Sha, J.E. Angelo, N.R. Moody, Correction: Trapping of hydrogen to lattice defects in nickel, Modelling Simul. Mater. Sci. Eng. 5 (6) (1997) 651–652.
[112] R.S. Elliott, Morse potential (shifted) for Al by Girifalco and Weizer (1959) using a high-accuracy cutoff distance v004, 2020, http://dx.doi.org/10.25950/45d9848f, OpenKIM.
[113] M.I. Pascuet, J.R. Fernández, Atomic interaction of the MEAM type for the study of intermetallics in the Al-U alloy, J. Nucl. Mater. 467 (2015) 229–239.
[114] X. Zhou, EAM potential (LAMMPS cubic hermite tabulation) for Al developed by Zhou, Johnson and Wadley (2004) v005, 2018, http://dx.doi.org/10.25950/ebdd9e47, OpenKIM.
[115] J.E. Angelo, N.R. Moody, M.I. Baskes, Trapping of hydrogen to lattice defects in nickel, Modelling Simul. Mater. Sci. Eng. 3 (3) (1995) 289.
[116] J.B. Sturgeon, B.B. Laird, Adjusting the melting point of a model system via Gibbs–Duhem integration: Application to a model of aluminum, Phys. Rev. B 62 (2000) 14720–14727.
[117] A. Landa, Glue potential (LAMMPS cubic hermite tabulation) for the Al-Pb system developed by Landa et al. (2000) v005, 2018, http://dx.doi.org/10.25950/d9f84889, OpenKIM.
[118] E. Tadmor, EAM potential (LAMMPS cubic hermite tabulation) for the Al-Co system developed by Pun, Yamakov and Mishin (2013) v000, 2018, http://dx.doi.org/10.25950/328bd9cb, OpenKIM.
[119] A. Mahata, T. Mukhopadhyay, M.A. Zaeem, Modified embedded-atom method interatomic potentials for Al-Cu, Al-Fe and Al-Ni binary alloys: From room temperature to melting point, Comput. Mater. Sci. 201 (2022) 110902.
[120] B.-J. Lee, J.-H. Shim, M. Baskes, Semiempirical atomic potentials for the fcc metals Cu, Ag, Au, Ni, Pd, Pt, Al, and Pb based on first and second nearest-neighbor modified embedded atom method, Phys. Rev. B 68 (14) (2003) 144112.
[121] S. Sun, B.R. Ramachandran, C.D. Wick, MEAM potential for TiAl alloys developed by Sun et al. (2018) v001, 2021, http://dx.doi.org/10.25950/b3c76733, OpenKIM.
[122] F. Apostol, Y. Mishin, Interatomic potential for the Al-Cu system, Phys. Rev. B 83 (2011) 054116.
[123] S.-P. Kim, EAM potential (LAMMPS cubic hermite tabulation) for the Al-Cu system developed by Cai and Ye (1996) v005, 2018, http://dx.doi.org/10.25950/73668fb7, OpenKIM.
[124] M.I. Baskes, EAM potential (LAMMPS cubic hermite tabulation) for the Ni-Al-H system developed by Angelo, Moody and Baskes (1995) v005, 2018, http://dx.doi.org/10.25950/3ea7788d, OpenKIM.
[125] E. Tadmor, EAM potential (LAMMPS cubic hermite tabulation) for the Ni-Al-Co system developed by Pun, Yamakov and Mishin (2013) v000, 2018, http://dx.doi.org/10.25950/48e9959e, OpenKIM.
[126] X. Zhou, R. Johnson, H. Wadley, Misfit-energy-increasing dislocations in vapor-deposited CoFe/NiFe multilayers, Phys. Rev. B 69 (14) (2004) 144113.
[127] A. Landa, P. Wynblatt, D.J. Siegel, J.B. Adams, O.N. Myrasov, X.-Y. Liu, Development of glue-type potentials for the Al–Pb system: phase diagram calculation, Acta Mater. 48 (8) (2000) 1753–1761.
[128] J.-H. Shim, W.-S. Ko, K.-H. Kim, H.-S. Lee, Y.-S. Lee, J.-Y. Suh, Y.W. Cho, B.-J. Lee, Prediction of hydrogen permeability in V–Al and V–Ni alloys, J. Membr. Sci. 430 (2013) 234–241.
[129] R.S. Elliott, Morse potential (shifted) for Al by Girifalco and Weizer (1959) using a medium-accuracy cutoff distance v004, 2020, http://dx.doi.org/10.25950/474ccb33, OpenKIM.
[130] G. Plummer, H.J. Rathod, A. Srivastava, M. Radovic, T. Ouisse, M. Yildizhan, P.O.A. Persson, K. Lambrinou, M.W. Barsoum, G.J. Tucker, Tersoff-style three-body potential for TiAlC developed by Plummer et al. (2021) v000, 2022, http://dx.doi.org/10.25950/7fbedfa8, OpenKIM.
[131] G.-U. Jeong, C.S. Park, H.-S. Do, S.-M. Park, B.-J. Lee, Second nearest-neighbor modified embedded-atom method interatomic potentials for the Pd-M (M=Al, Co, Cu, Fe, Mo, Ni, Ti) binary systems, CALPHAD 62 (2018) 172–186.
[132] G. Almyras, D. Sangiovanni, K. Sarakinos, MEAM potential for the N-Al-Ti system developed by Almyras et al. v001, 2021, http://dx.doi.org/10.25950/7f6ac722, OpenKIM.
[133] J. Schiotz, Effective Medium Theory (EMT) potential driver v004, 2019, http://dx.doi.org/10.25950/7e5b8be7, OpenKIM.
[134] W.-S. Ko, J.-H. Shim, B.-J. Lee, MEAM Potential for the Al-H system developed by Ko, Shim, and Lee (2011) v001, 2021, http://dx.doi.org/10.25950/f365e432, OpenKIM.
[135] X.-Y. Liu, J. Adams, Grain-boundary segregation in Al-10%Mg alloys at hot working temperatures, Acta Mater. 46 (10) (1998) 3467–3476.
[136] E. Tadmor, LAMMPS ADP potential for Al-Cu developed by Apostol and Mishin (2011) v000, 2019, http://dx.doi.org/10.25950/acf55448, OpenKIM.
[137] Y. Mishin, EAM potential (LAMMPS cubic hermite tabulation) for the B2-NiAl compound developed by Mishin, Mehl, and Papaconstantopoulos (2002) v005, 2018, http://dx.doi.org/10.25950/46227396, OpenKIM.
[138] T. Brink, A.P. Thompson, D.E. Farrell, M. Wen, J. Tersoff, J. Nord, K. Albe, P. Erhart, K. Nordlund, J.F. Ziegler, J.P. Biersack, U. Littmark, Model driver for Tersoff-style potentials ported from LAMMPS v005, 2021, http://dx.doi.org/10.25950/9a7dc96c, OpenKIM.
[139] V. Zhakhovskii, N. Inogamov, Y. Petrov, S. Ashitkov, K. Nishihara, Molecular dynamics simulation of femtosecond ablation and spallation with different interatomic potentials, Appl. Surf. Sci. 255 (24) (2009) 9592–9596, Proceedings of the Sixth International Conference onPhoto-Excited Processes and Applications(6-ICPEPA).
[140] B. Jelinek, S. Groh, M.F. Horstemeyer, J. Houze, S.-G. Kim, G.J. Wagner, A. Moitra, M.I. Baskes, MEAM potential for Al-Si-Mg-Cu-Fe alloys developed by Jelinek et al. (2012) v001, 2021, http://dx.doi.org/10.25950/5eca3b88, OpenKIM.
[141] M. Mendelev, D. Srolovitz, G. Ackland, S. Han, Effect of Fe segregation on the migration of a non-symmetric $\sigma 5$ tilt grain boundary in Al, J. Mater. Res. 20 (1) (2005) 208–218.
[142] H. Song, M.I. Mendelev, Molecular dynamics study of mechanism of solid–liquid interface migration and defect formation in Al3Sm alloy, JOM 73 (8) (2021) 2312–2319.
[143] A. Landa, P. Wynblatt, D.J. Siegel, J.B. Adams, O.N. Myrasov, X.-Y. Liu, Corrigendum: Development of glue-type potentials for the Al–Pb system: phase diagram calculation, Acta Mater. 48 (13) (2000) 3621.
[144] G.A. Almyras, D.G. Sangiovanni, K. Sarakinos, Semi-empirical force-field model for the Ti1-xAlxN ($0 \leq x \leq 1$) system, Materials 12 (2) (2019).
[145] Y. Mishin, EAM potential (LAMMPS cubic hermite tabulation) for Al developed by Zope and Mishin (2003) v005, 2018, http://dx.doi.org/10.25950/26dbac6e, OpenKIM.
[146] R.R. Zope, Y. Mishin, Interatomic potentials for atomistic simulations of the Ti-Al system, Phys. Rev. B 68 (2) (2003) 024102.
[147] W.-P. Dong, H.-K. Kim, W.-S. Ko, B.-M. Lee, B.-J. Lee, MEAM Potential for the Co-Al system developed by Dong et al. (2012) v001, 2021, http://dx.doi.org/10.25950/f9ed378c, OpenKIM.
[148] G.P. Pun, V. Yamakov, Y. Mishin, Interatomic potential for the ternary Ni–Al–Co system and application to atomistic modeling of the B2–L10 martensitic transformation, Modelling Simul. Mater. Sci. Eng. 23 (6) (2015) 065006.
[149] E. Tadmor, Glue potential (EAM-style) (LAMMPS cubic hermite tabulation) for Al developed by Ercolessi and Adams (1994) v003, 2020, http://dx.doi.org/10.25950/bc2d2486, OpenKIM.
[150] Y.-K. Kim, H.-K. Kim, W.-S. Jung, B.-J. Lee, Atomistic modeling of the Ti–Al binary system, Comput. Mater. Sci. 119 (2016) 1–8.

[151] W.-S. Ko, J.-H. Shim, B.-J. Lee, Atomistic modeling of the Al–H and Ni–H systems, J. Mater. Res. 26 (12) (2011) 1552–1560.

[152] Y. Mishin, M.J. Mehl, D.A. Papaconstantopoulos, Embedded-atom potential for B2–NiAl, Phys. Rev. B 65 (2002) 224114.

[153] J.A. Zimmerman, J.M. Winey, Y.M. Gupta, Elastic anisotropy of shocked aluminum single crystals: Use of molecular dynamics simulations, Phys. Rev. B 83 (2011) 184113.

[154] X.-Y. Liu, C.-L. Liu, L. Borucki, A new investigation of copper's role in enhancing Al-Cu interconnect electromigration resistance from an atomistic view, Acta Mater. 47 (11) (1999) 3227–3231.

[155] M.I. Mendelev, M. Asta, M.J. Rahman, J.J. Hoyt, Development of interatomic potentials appropriate for simulation of solid–liquid interface properties in Al–Mg alloys, Phil. Mag. 89 (34–36) (2009) 3269–3285.

[156] J. Cai, Y.Y. Ye, Simple analytical embedded-atom-potential model including a long-range force for fcc metals and their alloys, Phys. Rev. B 54 (1996) 8398–8410.

[157] E. Tadmor, EAM potential (LAMMPS cubic hermite tabulation) for Al developed by Zhou, Johnson, and Wadley (2004); NIST retabulation, 2018, http://dx.doi.org/10.25950/c775fc98, OpenKIM.

[158] Y. Mishin, EAM potential (LAMMPS cubic hermite tabulation) for the Ni-Al system developed by Mishin (2004) v005, 2018, http://dx.doi.org/10.25950/58d3fdeb, OpenKIM.

[159] D.E. Dickel, M.I. Baskes, I. Aslam, C.D. Barrett, MEAM potential for Mg-Al-Zn alloys developed by Dickel et al. (2018) v001, 2021, http://dx.doi.org/10.25950/7579be8a, OpenKIM.

[160] S. Sun, B.R. Ramachandran, C.D. Wick, Solid, liquid, and interfacial properties of TiAl alloys: parameterization of a new modified embedded atom method model, J. Phys.: Condens. Matter 30 (7) (2018) 075002.

[161] W.-P. Dong, H.-K. Kim, W.-S. Ko, B.-M. Lee, B.-J. Lee, Atomistic modeling of pure Co and Co–Al system, CALPHAD 38 (2012) 7–16.

[162] R.S. Elliott, EAM Model Driver for tabulated potentials with cubic Hermite spline interpolation as used in LAMMPS v005, 2018, http://dx.doi.org/10.25950/68defa36, OpenKIM.

[163] Y. Mishin, Atomistic modeling of the $\gamma$ and $\gamma$'-phases of the Ni-Al system, Acta Mater. 52 (6) (2004) 1451–1467.

[164] A.C. e Silva, J. Agren, M.T. Clavaguera-Mora, D. Djurovic, T. Gomez-Acebo, B.-J. Lee, Z.-K. Liu, A.P. Miodownik, H.J. Seifert, MEAM Potential for the Al-Ni system developed by Silva et al. (2007) v001, 2021, http://dx.doi.org/10.25950/d75ae573, OpenKIM.

[165] E. Tadmor, EAM potential (LAMMPS cubic hermite tabulation) for Al developed by Zhakhovsky et al. (2009) v000, 2018, http://dx.doi.org/10.25950/c3a79c52, OpenKIM.

[166] A. Mahata, T. Mukhopadhyay, M.A. Zaeem, MEAM Potential for the Al-Ni system developed by Mahata, Mukhopadhyay and Asle Zaeem (2022) v000, 2022, http://dx.doi.org/10.25950/da2ed6fb, OpenKIM.

[167] D.E. Dickel, M.I. Baskes, I. Aslam, C.D. Barrett, New interatomic potential for Mg–Al–Zn alloys with specific application to dilute Mg-based alloys, Modelling Simul. Mater. Sci. Eng. 26 (4) (2018) 045010.

[168] R.S. Elliott, Morse potential (shifted) for Cu by Girifalco and Weizer (1959) using a low-accuracy cutoff distance v004, 2020, http://dx.doi.org/10.25950/d44ce6cb, OpenKIM.

[169] M.I. Mendelev, Finnis–Sinclair potential (LAMMPS cubic hermite tabulation) for the Cu-Zr system developed by Mendelev, Sordelet and Kramer (2007) v005, 2018, http://dx.doi.org/10.25950/8556dbaf, OpenKIM.

[170] O. Deluigi, R. Pasianot, F. Valencia, A. Caro, D. Farkas, E. Bringa, Simulations of primary damage in a High Entropy Alloy: Probing enhanced radiation resistance, Acta Mater. 213 (2021) 116951.

[171] E. Asadi, M.A. Zaeem, S. Nouranian, M.I. Baskes, Two-phase solid–liquid coexistence of Ni, Cu, and Al by molecular dynamics simulations using the modified embedded-atom method, Acta Mater. 86 (2015) 169–181.

[172] N.P. Bailey, J. Schiøtz, K.W. Jacobsen, Erratum: Simulation of Cu-Mg metallic glass: Thermodynamics and structure, Phys. Rev. B 96 (2017) 059904.

[173] R.S. Elliott, R.E. Johnson, EAM potential (analytical nearest-neighbor) for Cu developed by Johnson (1988) v003, 2022, http://dx.doi.org/10.25950/26b6f589, OpenKIM.

[174] M.I. Mendelev, Finnis–Sinclar potential (LAMMPS cubic hermite tabulation) for liquid and amorphous Cu-Zr alloys developed by Mendelev et al. (2009) v005, 2018, http://dx.doi.org/10.25950/2f5abf6e, OpenKIM.

[175] V. Borovikov, M.I. Mendelev, A.H. King, Effects of stable and unstable stacking fault energy on dislocation nucleation in nano-crystalline metals, Modelling Simul. Mater. Sci. Eng. 24 (8) (2016) 085017.

[176] B. Onat, EAM potential (LAMMPS cubic hermite tabulation) for Cu-Ni alloys developed by Onat and Durukanoglu (2014) v005, 2018, http://dx.doi.org/10.25950/e2733dc9, OpenKIM.

[177] G.J. Ackland, Finnis–Sinclair potential (LAMMPS cubic hermite tabulation) for Cu developed by Ackland et al. (1987) v005, 2018, http://dx.doi.org/10.25950/7fe84e8c, OpenKIM.

[178] G.-U. Jeong, C.S. Park, H.-S. Do, S.-M. Park, B.-J. Lee, MEAM potential for the Pd-Cu system developed by Jeong et al. (2018) v001, 2021, http://dx.doi.org/10.25950/d8bd8e85, OpenKIM.

[179] S.A. Etesami, E. Asadi, Molecular dynamics for near melting temperatures simulations of metals using modified embedded-atom method, J. Phys. Chem. Solids 112 (2018) 61–72.

[180] E. Tadmor, Finnis–Sinclair potential (LAMMPS cubic hermite tabulation) for Cu developed by Ackland and Vitek (1990) v000, 2018, http://dx.doi.org/10.25950/36d99e43, OpenKIM.

[181] J. Wang, S.-H. Oh, B.-J. Lee, MEAM potential for the Cu-Co system developed by Wang et al. (2020) v001, 2021, http://dx.doi.org/10.25950/fce862f7, OpenKIM.

[182] E. Tadmor, EAM potential (LAMMPS cubic hermite tabulation) for the Cu-Ta system developed by Zhou, Johnson, and Wadley (2004); NIST retabulation v000, 2018, http://dx.doi.org/10.25950/fbcd3df9, OpenKIM.

[183] Y. Mishin, EAM potential (LAMMPS cubic hermite tabulation) for Cu developed by Mishin, Mehl and Papaconstantopoulos (2001) v005, 2018, http://dx.doi.org/10.25950/bbcadadf, OpenKIM.

[184] G.J. Ackland, G. Tichy, V. Vitek, M.W. Finnis, Simple N-body potentials for the noble metals and nickel, Phil. Mag. A 56 (6) (1987) 735–756.

[185] E. Tadmor, Finnis–Sinclair potential (LAMMPS cubic hermite tabulation) for Cu developed by Ackland et al. (1987), version 2 refitted for radiation studies v000, 2018, http://dx.doi.org/10.25950/492fc38f, OpenKIM.

[186] A. Agrawal, R. Mirzaeifar, MEAM potential for Cu-C composites developed by Agrawal and Mirzaeifar (2021) v001, 2021, http://dx.doi.org/10.25950/ba346aba, OpenKIM.

[187] Y. Mishin, EAM potential (LAMMPS cubic hermite tabulation) for the Cu-Ag system developed by Williams et al. (2006) v000, 2018, http://dx.doi.org/10.25950/d255748d, OpenKIM.

[188] R.A. Johnson, Analytic nearest-neighbor model for fcc metals, Phys. Rev. B 37 (1988) 3924–3931.

[189] X. Zhou, EAM potential (LAMMPS cubic hermite tabulation) for Cu developed by Zhou, Johnson and Wadley (2004) v005, 2018, http://dx.doi.org/10.25950/dd4e93a7, OpenKIM.

[190] L.P. Adrien Gola, EAM potential (LAMMPS cubic hermite tabulation) for Cu-Au alloys developed by Gola and Pastewka (2018) v000, 2020, http://dx.doi.org/10.25950/d7cdbeb9, OpenKIM.

[191] M.I. Mendelev, M.J. Kramer, R.T. Ott, D.J. Sordelet, D. Yagodin, P. Popel, Development of suitable interatomic potentials for simulation of liquid and amorphous Cu–Zr alloys, Phil. Mag. 89 (11) (2009) 967–987.

[192] M.I. Mendelev, Finnis–Sinclair potential (LAMMPS cubic hermite tabulation) for Cu with improved stacking fault energy developed by Mendelv and King (2013) v005, 2018, http://dx.doi.org/10.25950/34748b8d, OpenKIM.

[193] M.I. Mendelev, A.H. King, The interactions of self-interstitials with twin boundaries, Phil. Mag. 93 (10–12) (2013) 1268–1278.

[194] D. Farkas, A. Caro, Model interatomic potentials and lattice strain in a high-entropy alloy, J. Mater. Res. 33 (19) (2018) 3218–3225.

[195] M.I. Mendelev, Y. Sun, F. Zhang, C.Z. Wang, K.M. Ho, Development of a semi-empirical potential suitable for molecular dynamics simulation of vitrification in Cu-Zr alloys, J. Chem. Phys. 151 (21) (2019) 214502.

[196] E. Tadmor, EAM potential (LAMMPS cubic hermite tabulation) for the Cu-Ag-Au system developed by Zhou, Johnson and Wadley (2004); NIST retabulation v000, 2018, http://dx.doi.org/10.25950/d77528cf, OpenKIM.

[197] M.I. Mendelev, M.J. Kramer, C.A. Becker, M. Asta, Analysis of semi-empirical interatomic potentials appropriate for simulation of crystalline and liquid Al and Cu, Phil. Mag. 88 (12) (2008) 1723–1750.

[198] O. Deluigi, R.C. Pasianot, F.J. Valencia, A. Caro, D. Farkas, E. Bringa, EAM potential (LAMMPS cubic hermite tabulation) for FeNiCrCoCu developed by Deluigi et al. (2021) v000, 2021, http://dx.doi.org/10.25950/23f4f7cf, OpenKIM.

[199] Y.-M. Kim, B.-J. Lee, A modified embedded-atom method interatomic potential for the Cu–Zr system, J. Mater. Res. 23 (4) (2008) 1095–1104.

[200] G.J. Ackland, V. Vitek, Many-body potentials and atomic-scale relaxations in noble-metal alloys, Phys. Rev. B 41 (1990) 10324–10333.

[201] E. Tadmor, LAMMPS ADP potential for the Cu-Ta system developed by Pun et al. (2015) v000, 2019, http://dx.doi.org/10.25950/4ea3486d, OpenKIM.

[202] M.I. Mendelev, D.J. Sordelet, M.J. Kramer, Using atomistic computer simulations to analyze X-ray diffraction data from metallic glasses, J. Appl. Phys. 102 (4) (2007) 043501.

[203] J. Schiotz, EMT potential for Cu-Mg metallic glasses developed by Bailey, Schiotz, and Jacobsen (2004) v001, 2019, http://dx.doi.org/10.25950/dfe6edcd, OpenKIM.

[204] B.-J. Lee, J.-H. Shim, M.I. Baskes, MEAM potential for Cu developed by Lee, Shim, and Baskes (2003) v000, 2022, http://dx.doi.org/10.25950/ca58e4b9, OpenKIM.

[205] D. Farkas, A. Caro, EAM potential (LAMMPS cubic hermite tabulation) for the Fe-Ni-Cr-Co-Cu system developed by Farkas and Caro (2018) v000, 2022, http://dx.doi.org/10.25950/8c2ffcf6, OpenKIM.

[206] P.L. Williams, Y. Mishin, J.C. Hamilton, An embedded-atom potential for the Cu–Ag system, Modelling Simul. Mater. Sci. Eng. 14 (5) (2006) 817.

[207] G.J. Wagner, MEAM potential for Cu developed by Wagner (2007) v001, 2021, http://dx.doi.org/10.25950/cefcc47a, OpenKIM.

[208] G. Bonny, R.C. Pasianot, N. Castin, L. Malerba, Ternary Fe–Cu–Ni many-body potential to model reactor pressure vessel steels: First validation by simulated thermal annealing, Phil. Mag. 89 (34–36) (2009) 3531–3546.
[209] A. Gola, L. Pastewka, Embedded atom method potential for studying mechanical properties of binary Cu-Au alloys, Modelling Simul. Mater. Sci. Eng. 26 (2018) 055006.
[210] X.-G. Li, C. Hu, C. Chen, Z. Deng, J. Luo, S.P. Ong, Quantum-accurate spectral neighbor analysis potential models for Ni-Mo binary alloys and fcc metals, Phys. Rev. B 98 (9) (2018) 094104.
[211] J. Wang, S.-H. Oh, B.-J. Lee, MEAM potential for the Cu-Mo system developed by Wang et al. (2020) v001, 2021, http://dx.doi.org/10.25950/de2d8bd4, OpenKIM.
[212] A.S.M. Miraz, N. Dhariwal, W. Meng, B.R. Ramachandran, C.D. Wick, MEAM potential for Ti/TiN and Cu/TiN interfaces developed by Miraz et al. (2020) v001, 2021, http://dx.doi.org/10.25950/bc3a2244, OpenKIM.
[213] Y.-M. Kim, B.-J. Lee, MEAM potential for the Cu-Zr system developed by Kim and Lee (2008) v000, 2022, http://dx.doi.org/10.25950/7b3af95a, OpenKIM.
[214] K.-H. Kang, I. Sa, J.-C. Lee, E. Fleury, B.-J. Lee, Atomistic modeling of the Cu–Zr–Ag bulk metallic glass system, Scr. Mater. 61 (8) (2009) 801–804.
[215] E. Asadi, M.A. Zaeem, S. Nouranian, M.I. Baskes, MEAM potential for Cu developed by Asadi et al. (2015) v001, 2021, http://dx.doi.org/10.25950/9e752744, OpenKIM.
[216] J. Wang, S.-H. Oh, B.-J. Lee, MEAM potential for the Cu-Mo system developed by Wang, Oh, and Lee (2020) v001, 2021, http://dx.doi.org/10.25950/52c4c86f, OpenKIM.
[217] B. Onat, S. Durukanoğlu, An optimized interatomic potential for CuNi alloys with the embedded-atom method, J. Phys.: Condens. Matter 26 (3) (2014) 035404.
[218] Y. Afshar, Spectral neighbor analysis potential (SNAP) model driver v000, 2019, http://dx.doi.org/10.25950/f4fae493, OpenKIM.
[219] A.S.M. Miraz, N. Dhariwal, W. Meng, B.R. Ramachandran, C.D. Wick, Development and application of interatomic potentials to study the stability and shear strength of Ti/TiN and Cu/TiN interfaces, Mater. Des. 196 (2020) 109123.
[220] S.-A. Etesami, E. Asadi, MEAM potential for Cu developed by Etesami and Asadi (2018) v001, 2021, http://dx.doi.org/10.25950/93eb9c9f, OpenKIM.
[221] A. Agrawal, R. Mirzaeifar, Copper-graphene composites; developing the MEAM potential and investigating their mechanical properties, Comput. Mater. Sci. 188 (2021) 110204.
[222] E. Tadmor, EAM potential (LAMMPS cubic hermite tabulation) for the Cu-Ta system developed by Zhou, Johnson, and Wadley (2004) v000, 2018, http://dx.doi.org/10.25950/4482a6f2, OpenKIM.
[223] F. Fischer, G. Schmitz, S.M. Eich, A systematic study of grain boundary segregation and grain boundary formation energy using a new copper–nickel embedded-atom potential, Acta Mater. 176 (2019) 220–231.
[224] Y. Mishin, M.J. Mehl, D.A. Papaconstantopoulos, A.F. Voter, J.D. Kress, Structural stability and lattice defects in copper: Ab initio, tight-binding, and embedded-atom calculations, Phys. Rev. B 63 (2001) 224106.
[225] F. Fischer, G. Schmitz, S.M. Eich, EAM potential for Cu-Ni developed by Fischer et al. (2019) v000, 2021, http://dx.doi.org/10.25950/ca482d5d, OpenKIM.
[226] A. Păduraru, A. Kenoufi, N.P. Bailey, J. Schiøtz, An interatomic potential for studying CuZr bulk metallic glasses, Adv. Eng. Mater. 9 (6) (2007) 505–508.
[227] J.-S. Kim, D. Seol, J. Ji, H.-S. Jang, B.-J. Lee, MEAM potential for the Pt-Cu system developed by Kim and Lee (2017) v001, 2021, http://dx.doi.org/10.25950/47aad667, OpenKIM.
[228] R.S. Elliott, Morse potential (shifted) for Cu by Girifalco and Weizer (1959) using a medium-accuracy cutoff distance v004, 2020, http://dx.doi.org/10.25950/7c62475e, OpenKIM.
[229] K.-H. Kang, I. Sa, J.-C. Lee, E. Fleury, B.-J. Lee, MEAM potential for the Zr-Ag-Cu system developed by Kang et al. (2009) v001, 2021, http://dx.doi.org/10.25950/d596fc7e, OpenKIM.
[230] G.P. Pun, K. Darling, L. Kecskes, Y. Mishin, Angular-dependent interatomic potential for the Cu–Ta system and its application to structural stability of nano-crystalline alloys, Acta Mater. 100 (2015) 377–391.
[231] E. Tadmor, EAM potential (LAMMPS cubic hermite tabulation) for Cu developed by Zhou, Wadley and Johnson (2001) v000, 2018, http://dx.doi.org/10.25950/4cfacf76, OpenKIM.
[232] J. Wang, S.-H. Oh, B.-J. Lee, Second-nearest-neighbor modified embedded-atom method interatomic potential for Cu-M (M=Co, Mo) binary systems, Comput. Mater. Sci. 178 (2020) 109627.
[233] N.P. Bailey, J. Schiøtz, K.W. Jacobsen, Simulation of Cu-Mg metallic glass: Thermodynamics and structure, Phys. Rev. B 69 (2004) 144205.
[234] X. Li, A spectral neighbor analysis potential for Cu developed by Xiangguo Li (2019) v000, 2020, http://dx.doi.org/10.25950/c469334f, OpenKIM.
[235] R.S. Elliott, Morse potential (shifted) for Cu by Girifalco and Weizer (1959) using a high-accuracy cutoff distance v004, 2020, http://dx.doi.org/10.25950/6cbaeee8, OpenKIM.
[236] M. Mendelev, Finnis–Sinclair potential for the Cu-Zr system developed by Mendelev et al. (2019) v000, 2020, http://dx.doi.org/10.25950/9ad8e944, OpenKIM.
[237] M.I. Mendelev, EAM potential (LAMMPS cubic hermite tabulation) for Cu solidification developed by Mendelev et al. (2008) v005, 2018, http://dx.doi.org/10.25950/a557ef55, OpenKIM.
[238] G. Bonny, EAM potential (LAMMPS cubic hermite tabulation) for Fe-Cu-Ni reactor pressure vessel steels developed by Bonny et al. (2009) v005, 2018, http://dx.doi.org/10.25950/23db26d9, OpenKIM.
[239] H.H. Wu, D.R. Trinkle, Cu/Ag EAM potential optimized for heteroepitaxial diffusion from ab initio data, Comput. Mater. Sci. 47 (2) (2009) 577–583.
[240] M.I. Mendelev, E.B. Tadmor, EAM potential for Cu-Zr developed by Mendelev (2019) v000, 2020, http://dx.doi.org/10.25950/e3229f77, OpenKIM.
[241] E. Tadmor, Finnis–Sinclair potential (LAMMPS cubic hermite tabulation) for the Cu-Zr system developed by Borovikov, Mendelev and King (2016) v000, 2018, http://dx.doi.org/10.25950/e49bf93d, OpenKIM.
[242] J. Schiotz, EMT potential for Cu-Zr metallic glasses developed by Paduraru et al. (2007) v001, 2019, http://dx.doi.org/10.25950/82d2cfd9, OpenKIM.
[243] J. Wang, S.-H. Oh, B.-J. Lee, MEAM potential for the Cu-Co system developed by Wang, Oh, and Lee (2020) v001, 2021, http://dx.doi.org/10.25950/4b4ddb25, OpenKIM.
[244] E. Tadmor, EAM potential (LAMMPS cubic hermite tabulation) for Cu developed by Zhou, Johnson, and Wadley (2004); NIST retabulation v000, 2018, http://dx.doi.org/10.25950/885ad6aa, OpenKIM.
[245] J. Schiotz, EMT potential for Cu developed by Jacobsen, Stoltze, and Norskov (1996) v001, 2019, http://dx.doi.org/10.25950/77995a76, OpenKIM.
[246] H. Wu, EAM potential (LAMMPS cubic hermite tabulation) for the Cu-Ag system developed by Wu and Trinkle (2009) v000, 2018, http://dx.doi.org/10.25950/67d335dd, OpenKIM.
[247] X. Zhou, EAM potential (LAMMPS cubic hermite tabulation) for Ni developed by Zhou, Johnson and Wadley (2004) v005, 2018, http://dx.doi.org/10.25950/35de8ef7, OpenKIM.
[248] X. Li, A spectral neighbor analysis potential for Ni developed by Xiangguo Li (2019) v000, 2020, http://dx.doi.org/10.25950/4e758263, OpenKIM.
[249] E. Asadi, M.A. Zaeem, S. Nouranian, M.I. Baskes, MEAM potential for Ni developed by Asadi et al. (2015) v001, 2021, http://dx.doi.org/10.25950/2be3b822, OpenKIM.
[250] G. Bonny, R.C. Pasianot, L. Malerba, Fe–Ni many-body potential for metallurgical applications, Modelling Simul. Mater. Sci. Eng. 17 (2) (2009) 025010.
[251] M.I. Mendelev, Finnis–Sinclair potential (LAMMPS cubic hermite tabulation) for Ni solidification developed by Mendelev et al. (2012) v05, 2018, http://dx.doi.org/10.25950/ebd6cbc4, OpenKIM.
[252] G. Bonny, EAM potential (LAMMPS cubic hermite tabulation) for the FeNi system developed by Bonny, Pasianot and Malerba (2009) v005, 2018, http://dx.doi.org/10.25950/e54b898a, OpenKIM.
[253] R.E. Stoller, A. Tamm, L.K. Béland, G.D. Samolyuk, G.M. Stocks, A. Caro, L.V. Slipchenko, Y.N. Osetsky, A. Aabloo, M. Klintenberg, Y. Wang, Impact of short-range forces on defect production from high-energy collisions, J. Chem. Theory Comput. 12 (6) (2016) 2871–2879, PMID: 27110927.
[254] C. Wu, B.-J. Lee, X. Su, MEAM potential for the Ni-Cr-Fe system developed by Wu, Lee, and Su (2017) v001, 2021, http://dx.doi.org/10.25950/9354c995, OpenKIM.
[255] E. Tadmor, Finnis–Sinclair potential (LAMMPS cubic hermite tabulation) for the Ni-Zr system developed by Wilson and Mendelev (2015) v000, 2018, http://dx.doi.org/10.25950/3c8ce3fd, OpenKIM.
[256] L.K. Béland, A. Tamm, S. Mu, G.D. Samolyuk, Y.N. Osetsky, A. Aabloo, M. Klintenberg, A. Caro, R.E. Stoller, Accurate classical short-range forces for the study of collision cascades in Fe-Ni-Cr, Comput. Phys. Comm. 219 (2017) 11–19.
[257] B.-J. Lee, J.-H. Shim, M.I. Baskes, MEAM potential for Ni developed by Lee, Shim, and Baskes (2003) v000, 2022, http://dx.doi.org/10.25950/7e999f59, OpenKIM.
[258] Y. Xu, G. Wang, P. Qian, Y. Su, Element segregation and thermal stability of Ni–Pd nanoparticles, J. Mater. Sci. 57 (14) (2022) 7384–7399.
[259] J. Schiotz, EMT potential for Ni developed by Jacobsen, Stolze, and Norskov (1996) v001, 2019, http://dx.doi.org/10.25950/ef22cbc3, OpenKIM.
[260] G.J. Wagner, MEAM potential for Ni developed by Wagner (2007) v001, 2021, http://dx.doi.org/10.25950/9fb66ca3, OpenKIM.
[261] S. Wilson, M. Mendelev, Anisotropy of the solid-liquid interface properties of the Ni-Zr B33 phase from molecular dynamics simulation, Phil. Mag. 95 (2) (2015) 224–241.
[262] W.-M. Choi, Y.H. Jo, S. Sohn, S. Lee, B.-J. Lee, MEAM potential for the Co-Ni-Cr-Fe-Mn system developed by Choi et al., (2018) v001, 2021, http://dx.doi.org/10.25950/bc54d772, OpenKIM.
[263] E. Tadmor, LAMMPS ADP potential for Ni developed by Mishin et al. (2005) v000, 2019, http://dx.doi.org/10.25950/dd7328e8, OpenKIM.
[264] S. Kavousi, B.R. Novak, M.I. Baskes, M. Asle Zaeem, D. Moldovan, Modified embedded-atom method potential for high-temperature crystal-melt properties of Ti–Ni alloys and its application to phase field simulation of solidification, Modelling Simul. Mater. Sci. Eng. 28 (1) (2019) 015006.
[265] R.S. Elliott, Morse potential (shifted) for Ni by Girifalco and Weizer (1959) using a low-accuracy cutoff distance v004, 2020, http://dx.doi.org/10.25950/e9422396, OpenKIM.

[266] E. Tadmor, EAM potential (LAMMPS cubic hermite tabulation) for Ni developed by Zhou, Johnson, and Wadley (2004); NIST retabulation v000, 2018, http://dx.doi.org/10.25950/e858c268, OpenKIM.

[267] W.-S. Ko, B. Grabowski, J. Neugebauer, MEAM potential for Ni-Ti developed by Ko, Grabowski, and Neugebauer (2015) v001, 2021, http://dx.doi.org/10.25950/56bfbab4, OpenKIM.

[268] G.D. Samolyuk, L.K. Béland, G.M. Stocks, R.E. Stoller, EAM potential (LAMMPS cubic hermite tabulation) for the Ni-Pd system developed by Samolyuk et al. (2016) v000, 2022, http://dx.doi.org/10.25950/bbd6e8af, OpenKIM.

[269] J.-H. Shim, S.I. Park, Y.W. Cho, B.-J. Lee, Modified embedded-atom method calculation for the Ni–W system, J. Mater. Res. 18 (8) (2003) 1863–1867.

[270] R.E. Stoller, A. Tamm, L.K. Béland, G.D. Samolyuk, G.M. Stocks, A. Caro, L.V. Slipchenko, Y.N. Osetskiy, A. Aabloo, M. Klintenberg, Y. Wang, EAM potential (LAMMPS cubic hermite tabulation) for Ni developed by Stoller et al. (2016) v000, 2022, http://dx.doi.org/10.25950/442baec7, OpenKIM.

[271] W.-S. Ko, B. Grabowski, J. Neugebauer, Development and application of a Ni-Ti interatomic potential with high predictive accuracy of the martensitic phase transition, Phys. Rev. B 92 (2015) 134107.

[272] R.S. Elliott, EAM potential (cubic natural spline tabulation) for Ni developed by Angelo et al. (1995) modified by Dupuy for smooth derivatives v003, 2020, http://dx.doi.org/10.25950/73c8ccfd, OpenKIM.

[273] G.-U. Jeong, C.S. Park, H.-S. Do, S.-M. Park, B.-J. Lee, MEAM potential for the Pd-Ni system developed by Jeong et al. (2018) v001, 2021, http://dx.doi.org/10.25950/48cc2428, OpenKIM.

[274] Z. Pan, V. Borovikov, M.I. Mendelev, F. Sansoz, Development of a semi-empirical potential for simulation of Ni solute segregation into grain boundaries in Ag, Modelling Simul. Mater. Sci. Eng. 26 (7) (2018) 075004.

[275] L.K. Béland, C. Lu, Y.N. Osetskiy, G.D. Samolyuk, A. Caro, L. Wang, R.E. Stoller, Features of primary damage by high energy displacement cascades in concentrated Ni-based alloys, J. Appl. Phys. 119 (8) (2016).

[276] S.M. Foiles, J.J. Hoyt, EAM potential (LAMMPS cubic hermite tabulation) for Ni developed by Foiles and Hoyt (2006) v000, 2022, http://dx.doi.org/10.25950/72b7e9dc, OpenKIM.

[277] C. Wu, B.-J. Lee, X. Su, Modified embedded-atom interatomic potential for Fe-Ni, Cr-Ni and Fe-Cr-Ni systems, CALPHAD 57 (2017) 98–106.

[278] C. Wu, B.-J. Lee, X. Su, MEAM potential for the Ni-Cr system developed by Wu, Lee, and Su (2017) v001, 2021, http://dx.doi.org/10.25950/c7d4877a, OpenKIM.

[279] W.-M. Choi, Y.H. Jo, S.S. Sohn, S. Lee, B.-J. Lee, Understanding the physical metallurgy of the CoCrFeMnNi high-entropy alloy: an atomistic simulation study, npj Comput. Mater. 4 (2018) 1.

[280] M. Mendelev, M. Kramer, S. Hao, K. Ho, C. Wang, Development of interatomic potentials appropriate for simulation of liquid and glass properties of NiZr2 alloy, Phil. Mag. 92 (35) (2012) 4454–4469.

[281] Y. Xu, G. Wang, P. Qian, Y. Su, LAMMPS ADP potential for the Ni-Rh system developed by Xu et al. (2022) v000, 2022, http://dx.doi.org/10.25950/378777f4, OpenKIM.

[282] M.I. Mendelev, M.J. Kramer, S.G. Hao, K.M. Ho, C.Z. Wang, Development of interatomic potentials appropriate for simulation of liquid and glass properties of $NiZr_2$ alloy, Phil. Mag. 92 (35) (2012) 4454–4469.

[283] S.-A. Etesami, E. Asadi, MEAM potential for Ni developed by Etesami and Asadi (2018) v001, 2021, http://dx.doi.org/10.25950/e9fbd3dc, OpenKIM.

[284] Y. Zhang, R. Ashcraft, M.I. Mendelev, C.Z. Wang, K.F. Kelton, Experimental and molecular dynamics simulation study of structure of liquid and amorphous Ni62Nb38 alloy, J. Chem. Phys. 145 (20) (2016) 204505.

[285] E. Tadmor, EAM potential (LAMMPS cubic hermite tabulation) for the Ni-Co system developed by Pun, Yamakov and Mishin (2015) v000, 2018, http://dx.doi.org/10.25950/aeeef694, OpenKIM.

[286] G.D. Samolyuk, L.K. Béland, G.M. Stocks, R.E. Stoller, Electron–phonon coupling in Ni-based binary alloys with application to displacement cascade modeling, J. Phys.: Condens. Matter 28 (17) (2016) 175501.

[287] S.B. Maisel, W.-S. Ko, J.-L. Zhang, B. Grabowski, J. Neugebauer, Thermomechanical response of NiTi shape-memory nanoprecipitates in TiV alloys, Phys. Rev. Mater. 1 (2017) 033610.

[288] E. Tadmor, EAM potential (LAMMPS cubic hermite tabulation) for the Fe-Ni-Cr system developed by Bonny, Castin and Terentyev (2013) v000, 2018, http://dx.doi.org/10.25950/3e7879ea, OpenKIM.

[289] Y. Xu, G. Wang, P. Qian, Y. Su, LAMMPS ADP potential for the Ni-Pd system developed by Xu et al. (2022) v000, 2022, http://dx.doi.org/10.25950/b34ee4fe, OpenKIM.

[290] C. Wu, B.-J. Lee, X. Su, MEAM potential for the Ni-Fe system developed by Wu, Lee, and Su (2017) v001, 2021, http://dx.doi.org/10.25950/d9caac35, OpenKIM.

[291] L.K. Béland, C. Lu, Y.N. Osetskiy, G.D. Samolyuk, A. Caro, L. Wang, R.E. Stoller, EAM potential (LAMMPS cubic hermite tabulation) for the Ni-Co system developed by Beland et al. (2016) v000, 2022, http://dx.doi.org/10.25950/9884d9d7, OpenKIM.

[292] S.B. Maisel, W.-S. Ko, J.J.L. Zhang, B. Grabowski, J. Neugebauer, MEAM potential for V-Ni-Ti developed by Maisel et al. (2017) v001, 2021, http://dx.doi.org/10.25950/898d3737, OpenKIM.

[293] S.M. Foiles, J. Hoyt, Computation of grain boundary stiffness and mobility from boundary fluctuations, Acta Mater. 54 (12) (2006) 3351–3357.

[294] G.J. Ackland, Finnis–Sinclair potential (LAMMPS cubic hermite tabulation) for Ni developed by Ackland et al. (1987) v005, 2018, http://dx.doi.org/10.25950/7666385f, OpenKIM.

[295] L.K. Béland, A. Tamm, S. Mu, G.D. Samolyuk, Y.N. Osetskiy, A. Aabloo, M. Klintenberg, A. Caro, R.E. Stoller, EAM potential (LAMMPS cubic hermite tabulation) for the Fe-Ni-Cr system developed by Beland et al. (2017) v000, 2022, http://dx.doi.org/10.25950/3b5d96b4, OpenKIM.

[296] R.S. Elliott, Morse potential (shifted) for Ni by Girifalco and Weizer (1959) using a medium-accuracy cutoff distance v004, 2020, http://dx.doi.org/10.25950/4dc95deb, OpenKIM.

[297] Y. Xu, G. Wang, P. Qian, Y. Su, Element segregation and thermal stability of Ni-Rh nanoparticles, J. Solid State Chem. 311 (2022) 123096.

[298] Y. Mishin, M. Mehl, D. Papaconstantopoulos, Phase stability in the Fe-Ni system: Investigation by first-principles calculations and atomistic simulations, Acta Mater. 53 (15) (2005) 4029–4041.

[299] Z. Pan, V. Borovikov, M.I. Mendelev, F. Sansoz, EAM potential (LAMMPS cubic hermite tabulation) for the Ag-Ni system developed by Pan et al. (2018) v000, 2022, http://dx.doi.org/10.25950/baeb8352, OpenKIM.

[300] X.W. Zhou, M.E. Foster, R.B. Sills, An Fe-Ni-Cr embedded atom method potential for austenitic and ferritic systems, J. Comput. Chem. 39 (29) (2018) 2420–2431.

[301] J.-H. Shim, S.I. Park, Y.W. Cho, B.-J. Lee, MEAM potential for the Ni-W system developed by Shim et al. (2003) v001, 2021, http://dx.doi.org/10.25950/fadc325f, OpenKIM.

[302] E. Tadmor, Finnis–Sinclair potential (LAMMPS cubic hermite tabulation) for Ni developed by Ackland et al. (1987), version 2 refitted for radiation studies v000, 2018, http://dx.doi.org/10.25950/37ebcbaa, OpenKIM.

[303] J.-H. Shim, W.-S. Ko, K.-H. Kim, H.-S. Lee, Y.-S. Lee, J.-Y. Suh, Y.W. Cho, B.-J. Lee, MEAM potential for the Ni-V-H system developed by Shim et al. (2013) v001, 2021, http://dx.doi.org/10.25950/245f8695, OpenKIM.

[304] X. Zhou, M.E. Foster, R.B. Sills, EAM potential (LAMMPS cubic hermite tabulation) for Fe-Ni-Cr developed by Zhou, Foster and Sills (2018) v000, 2022, http://dx.doi.org/10.25950/e28aaa47, OpenKIM.

[305] J.-S. Kim, D. Seol, J. Ji, H.-S. Jang, B.-J. Lee, MEAM potential for the Pt-Ni system developed by Kim and Lee (2017) v001, 2021, http://dx.doi.org/10.25950/93e56677, OpenKIM.

[306] R.S. Elliott, Morse potential (shifted) for Ni by Girifalco and Weizer (1959) using a high-accuracy cutoff distance v004, 2020, http://dx.doi.org/10.25950/fc55a3bb, OpenKIM.

[307] R.S. Elliott, M. Wen, Cubic-natural-spline EAM model driver for tabulated potentials with cubic natural spline interpolation v002, 2018, http://dx.doi.org/10.25950/4cf7be5a, OpenKIM.

[308] X. Li, A spectral neighbor analysis potential for Ni-Mo developed by Xiangguo Li (2019) v000, 2020, http://dx.doi.org/10.25950/f3abd33c, OpenKIM.

[309] M. Mendelev, Finnis–Sinclair potential for the Fe-Ni-Cr system developed by Mendelev et al. (2020) v000, 2020, http://dx.doi.org/10.25950/538764d4, OpenKIM.

[310] M.I. Mendelev, Finnis–Sinclair potential (LAMMPS cubic hermite tabulation) for the Ni-Zr system developed by Mendelev et al. (2012) v005, 2018, http://dx.doi.org/10.25950/d7924336, OpenKIM.

[311] S. Kavousi, B.R. Novak, M.I. Baskes, M.A. Zaeem, D. Moldovan, MEAM potential for Ni-Ti alloys developed by Kavousi et al., (2019) v001, 2021, http://dx.doi.org/10.25950/ecf35cd6, OpenKIM.

[312] A. Tehranchi, EAM potential (LAMMPS cubic hermite tabulation) for Ni-H with enhanced binding of H atoms to Ni grain boundaries by Tehranchi and Curtin (2017) v003, 2018, http://dx.doi.org/10.25950/9f526e73, OpenKIM.

[313] E. Tadmor, Finnis–Sinclair potential (LAMMPS cubic hermite tabulation) for the Ni-Nb system developed by Zhang et al. (2016) v000, 2018, http://dx.doi.org/10.25950/72b4c275, OpenKIM.

[314] G. Bonny, N. Castin, D. Terentyev, Interatomic potential for studying ageing under irradiation in stainless steels: the FeNiCr model alloy, Modelling Simul. Mater. Sci. Eng. 21 (8) (2013) 085004.

[315] Y. Mishin, EAM potential (LAMMPS cubic hermite tabulation) for Ni developed by Mishin et al. (1999) v005, 2018, http://dx.doi.org/10.25950/a88dfc37, OpenKIM.

[316] I. Aslam, M.I. Baskes, D.E. Dickel, S. Adibi, B. Li, H. Rhee, M.A. Zaeem, M.F. Horstemeyer, MEAM potential for the Fe-Mn-Si-C system developed by Aslam et al. (2019) v001, 2021, http://dx.doi.org/10.25950/96a57792, OpenKIM.

[317] G. Bonny, R. Pasianot, D. Terentyev, L. Malerba, N. Castin, Interatomic Potential to Simulate Radiation Damage in Fe-Cr Alloys, Tech. Rep, SCK CEN, 2011.

[318] M.R. Gilbert, EAM potential (cubic tabulation) for Fe developed by Mendelev et al. (2003) v002, 2018, http://dx.doi.org/10.25950/6766e8a2, OpenKIM.

[319] P.A. Olsson, Semi-empirical atomistic study of point defect properties in BCC transition metals, Comput. Mater. Sci. 47 (1) (2009) 135–145.

[320] Y.-M. Kim, Y.-H. Shin, B.-J. Lee, MEAM potential for the Fe-Mn system developed by Kim, Shin, Lee (2009) v001, 2021, http://dx.doi.org/10.25950/beb4e5ff, OpenKIM.

[321] B.-J. Lee, MEAM potential for the Fe-C system developed by Lee (2008) v001, 2021, http://dx.doi.org/10.25950/e2f343aa, OpenKIM.

[322] M.R. Gilbert, Second generation EAM potential within the magnetic potential formalism with quintic interpolation v002, 2018, http://dx.doi.org/10.25950/ed3ceac9, OpenKIM.
[323] D.S. Karls, LAMMPS tersoff-ZBL potential for Fe-C developed by Henriksson, Björkas and Nordlund (2013) v000, 2019, http://dx.doi.org/10.25950/ebe5cf99, OpenKIM.
[324] W.-S. Ko, N.J. Kim, B.-J. Lee, MEAM potential for the Fe-P system developed by Ko, Kim, and Lee (2012) v001, 2021, http://dx.doi.org/10.25950/eca64e48, OpenKIM.
[325] H.-K. Kim, W.-S. Jung, B.-J. Lee, Modified embedded-atom method interatomic potentials for the Nb-C, Nb-N, Fe-Nb-C, and Fe-Nb-N systems, J. Mater. Res. 25 (7) (2010) 1288–1297.
[326] R.S. Elliott, Morse potential (shifted) for Fe by Girifalco and Weizer (1959) using a low-accuracy cutoff distance v004, 2020, http://dx.doi.org/10.25950/29eb9b72, OpenKIM.
[327] E. Tadmor, Finnis–Sinclair potential (LAMMPS cubic hermite tabulation) for Fe developed by Marinica (2011) v000, 2018, http://dx.doi.org/10.25950/74bc5eea, OpenKIM.
[328] M.R. Gilbert, EAM potential (2nd gen magnetic, quintic tabulation) for magnetic Fe developed by Chiesa et al. (2011) v002, 2018, http://dx.doi.org/10.25950/ce6a5ce5, OpenKIM.
[329] I. Sa, B.-J. Lee, MEAM potential for the Fe-Ti system developed by Sa and Lee (2008) v001, 2021, http://dx.doi.org/10.25950/728b47a3, OpenKIM.
[330] Y.-M. Kim, Y.-H. Shin, B.-J. Lee, Modified embedded-atom method interatomic potentials for pure Mn and the Fe–Mn system, Acta Mater. 57 (2) (2009) 474–482.
[331] E. Tadmor, EAM potential (LAMMPS cubic hermite tabulation) for Fe developed by Chamati et al. (2006) v000, 2018, http://dx.doi.org/10.25950/82c75aaa, OpenKIM.
[332] I. Sa, B.-J. Lee, Modified embedded-atom method interatomic potentials for the Fe-Nb and Fe-Ti binary systems, Scr. Mater. 59 (6) (2008) 595–598.
[333] M. Müller, P. Erhart, K. Albe, Analytic bond-order potential for bcc and fcc iron—comparison with established embedded-atom method potentials, J. Phys.: Condens. Matter 19 (32) (2007) 326220.
[334] G. Bonny, N. Castin, J. Bullens, A. Bakaev, T. Klaver, D. Terentyev, LAMMPS EAM potential for Fe-Cr-W developed by Bonny et al. (2013) v001, 2021, http://dx.doi.org/10.25950/a8d59af8, OpenKIM.
[335] W.-M. Choi, Y. Kim, D. Seol, B.-J. Lee, Modified embedded-atom method interatomic potentials for the Co-Cr, Co-Fe, Co-Mn, Cr-Mn and Mn-Ni binary systems, Comput. Mater. Sci. 130 (2017) 121–129.
[336] G.J. Ackland, EAM potential (LAMMPS cubic hermite tabulation) for the FeC system developed by Ackland and Hepburn (2008) v005, 2018, http://dx.doi.org/10.25950/a38f2843, OpenKIM.
[337] W.-S. Ko, N.J. Kim, B.-J. Lee, Atomistic modeling of an impurity element and a metal–impurity system: pure P and Fe–P system, J. Phys.: Condens. Matter 24 (22) (2012) 225002.
[338] R.S. Elliott, Morse potential (shifted) for Fe by Girifalco and Weizer (1959) using a high-accuracy cutoff distance v004, 2020, http://dx.doi.org/10.25950/c88bdaae, OpenKIM.
[339] R.E. Miller, EAM potential (LAMMPS cubic hermite tabulation) for Fe developed by Mendelev et al. (2003) v000, 2018, http://dx.doi.org/10.25950/4d284d74, OpenKIM.
[340] H.-K. Kim, W.-S. Jung, B.-J. Lee, MEAM potential for the Fe-Ti-C system developed by Kim, Jung, Lee (2009) v001, 2021, http://dx.doi.org/10.25950/fa2b964a, OpenKIM.
[341] J. Byggmästar, F.G. Granberg, LAMMPS Tersoff-ZBL potential for Fe developed by J. Byggmästar and Granberg (2020) v000, 2020, http://dx.doi.org/10.25950/436c99e7, OpenKIM.
[342] J. Byggmästar, M. Nagel, K. Albe, K.O.E. Henriksson, K. Nordlund, Tersoff-ZBL potential for FeO developed by Byggmastar et al. (2019) v000, 2022, http://dx.doi.org/10.25950/dc7b5aa7, OpenKIM.
[343] J. Kim, B.-J. Lee, MEAM potential for the Pt-Fe system developed by Kim, Koo, and Lee (2006) v001, 2021, http://dx.doi.org/10.25950/62426287, OpenKIM.
[344] S.L. Dudarev, P.M. Derlet, A 'magnetic' interatomic potential for molecular dynamics simulations, J. Phys.: Condens. Matter 17 (44) (2005) 7097–7118.
[345] M.R. Gilbert, EAM potential (magnetic, cubic tabulation) for magnetic Fe developed by Dudarev and Derlet (2005) v002, 2018, http://dx.doi.org/10.25950/eb4996de, OpenKIM.
[346] K.O.E. Henriksson, C. Björkas, K. Nordlund, Atomistic simulations of stainless steels: a many-body potential for the Fe-Cr-C system, J. Phys.: Condens. Matter 25 (44) (2013) 445401.
[347] M. Wen, EAM potential (LAMMPS cubic hermite tabulation) for the Fe-H system developed by Wen (2021) v000, 2022, http://dx.doi.org/10.25950/dd97869d, OpenKIM.
[348] M.I. Mendelev, Finnis–Sinclair potential (LAMMPS cubic hermite tabulation) for the Fe-P system developed by Ackland et al. (2004) v000, 2018, http://dx.doi.org/10.25950/cf64bcf2, OpenKIM.
[349] G.-U. Jeong, C.S. Park, H.-S. Do, S.-M. Park, B.-J. Lee, MEAM potential for the Pd-Fe system developed by Jeong et al. (2018) v001, 2021, http://dx.doi.org/10.25950/cf34963b, OpenKIM.
[350] M.R. Gilbert, EAM potential for magnetic bcc metals with cubic spline interpolation v002, 2018, http://dx.doi.org/10.25950/9776664f, OpenKIM.
[351] L. Malerba, M. Marinica, N. Anento, Bjoerkas, H. Nguyen, C. Domain, F. Djurabekova, P. Olsson, K. Nordlund, A. Serra, D. Terentyev, F. Willaime, C. Becquart, Comparison of empirical interatomic potentials for iron applied to radiation damage studies, J. Nucl. Mater. 406 (1) (2010) 19–38.
[352] I. Sa, B.-J. Lee, MEAM potential for the Nb-Fe system developed by Sa and Lee (2008) v001, 2021, http://dx.doi.org/10.25950/736336aa, OpenKIM.
[353] J. Kim, Y. Koo, B.-J. Lee, Modified embedded-atom method interatomic potential for the Fe–Pt alloy system, J. Mater. Res. 21 (1) (2006) 199–208.
[354] E. Tadmor, Finnis–Sinclair potential (LAMMPS cubic hermite tabulation) for Fe developed by Marinica (2007) v000, 2018, http://dx.doi.org/10.25950/6c8499d4, OpenKIM.
[355] G. Bonny, N. Castin, J. Bullens, A. Bakaev, T. Klaver, D. Terentyev, On the mobility of vacancy clusters in reduced activation steels: an atomistic study in the Fe–Cr–W model alloy, J. Phys.: Condens. Matter 25 (31) (2013) 315401.
[356] M. Mendelev, S. Han, D. Srolovitz, G. Ackland, D. Sun, M. Asta, Development of new interatomic potentials appropriate for crystalline and liquid iron, Philosophical magazine 83 (35) (2003) 3977–3994.
[357] M.I. Mendelev, EAM potential (LAMMPS cubic hermite tabulation) for Fe developed by Mendelev et al. (2003); Potential #5 v005, 2018, http://dx.doi.org/10.25950/b73f2bfe, OpenKIM.
[358] G. Bonny, R.C. Pasianot, D. Terentyev, L. Malerba, LAMMPS EAM potential for Fe-Cr developed by Bonny et al. (2011) v001, 2021, http://dx.doi.org/10.25950/d82afb9f, OpenKIM.
[359] A. Machová, G.J. Ackland, Dynamic overshoot in alpha-iron by atomistic simulations, Modelling Simul. Mater. Sci. Eng. 6 (5) (1998) 521–542.
[360] J. Byggmästar, M. Nagel, K. Albe, K.O.E. Henriksson, K. Nordlund, Analytical interatomic bond-order potential for simulations of oxygen defects in iron, J. Phys.: Condens. Matter 31 (21) (2019) 215401.
[361] J.R. Morris, R.S. Aga, V. Levashov, T. Egami, Many-body effects in bcc metals: An embedded atom model extension of the modified Johnson pair potential for iron, Phys. Rev. B 77 (2008) 174201.
[362] D.J. Hepburn, G.J. Ackland, Metallic-covalent interatomic potential for carbon in iron, Phys. Rev. B 78 (2008) 165115.
[363] B.-J. Lee, M.I. Baskes, H. Kim, Y.K. Cho, MEAM potential for Fe developed by Lee et al. (2001) v000, 2022, http://dx.doi.org/10.25950/85a9cb32, OpenKIM.
[364] M.I. Mendelev, S. Han, W.-j. Son, G.J. Ackland, D.J. Srolovitz, Simulation of the interaction between Fe impurities and point defects in V, Phys. Rev. B 76 (2007) 214105.
[365] M. Wen, A new interatomic potential describing Fe-H and H-H interactions in bcc iron, Comput. Mater. Sci. 197 (2021) 110640.
[366] Y. Sun, F. Zhang, M.I. Mendelev, R.M. Wentzcovitch, K.-M. Ho, Two-step nucleation of the Earth's inner core, Proc. Natl. Acad. Sci. 119 (2) (2022) e2113059119.
[367] R.S. Elliott, Morse potential (shifted) for Fe by Girifalco and Weizer (1959) using a medium-accuracy cutoff distance v004, 2020, http://dx.doi.org/10.25950/fe5a84a9, OpenKIM.
[368] I. Aslam, M. Baskes, D. Dickel, S. Adibi, B. Li, H. Rhee, M. Asle Zaeem, M. Horstemeyer, Thermodynamic and kinetic behavior of low-alloy steels: An atomic level study using an Fe-Mn-Si-C modified embedded atom method (MEAM) potential, Materialia 8 (2019) 100473.
[369] S. Chiesa, P.M. Derlet, S.L. Dudarev, H.V. Swygenhoven, Optimization of the magnetic potential for $\alpha$-Fe, J. Phys.: Condens. Matter 23 (20) (2011) 206001.
[370] E. Tadmor, EAM potential (LAMMPS cubic hermite tabulation) for the Fe-W system developed by Bonny et al. (2013) v000, 2018, http://dx.doi.org/10.25950/e7fa524a, OpenKIM.
[371] H.-K. Kim, W.-S. Jung, B.-J. Lee, MEAM potential for the Fe-Nb-C system developed by Kim and Lee (2010) v001, 2021, http://dx.doi.org/10.25950/aafda65d, OpenKIM.
[372] G.J. Ackland, Finnis–Sinclair potential (LAMMPS cubic hermite tabulation) for bcc Fe developed by Ackland et al. (1997) v005, 2018, http://dx.doi.org/10.25950/93837486, OpenKIM.
[373] H.-K. Kim, W.-S. Jung, B.-J. Lee, Modified embedded-atom method interatomic potentials for the Fe–Ti–C and Fe–Ti–N ternary systems, Acta Mater. 57 (11) (2009) 3140–3147.
[374] P.A.T. Olsson, EAM potential (LAMMPS cubic hermite tabulation) for Fe developed by Olsson (2009) v000, 2022, http://dx.doi.org/10.25950/bf295ec5, OpenKIM.
[375] G. Bonny, R. Pasianot, D. Terentyev, L. Malerba, Iron chromium potential to model high-chromium ferritic alloys, Phil. Mag. 91 (12) (2011) 1724–1746.
[376] S.M. Eich, D. Beinke, G. Schmitz, Embedded-atom potential for an accurate thermodynamic description of the iron–chromium system, Comput. Mater. Sci. 104 (2015) 185–192.
[377] G.J. Ackland, M.I. Mendelev, D.J. Srolovitz, S. Han, A.V. Barashev, Development of an interatomic potential for phosphorus impurities in $\alpha$-iron, J. Phys.: Condens. Matter 16 (27) (2004) S2629.
[378] Y. Sun, F. Zhang, M.I. Mendelev, R.M. Wentzcovitch, K.-M. Ho, EAM potential (LAMMPS cubic hermite tabulation) for Fe developed by Sun et al. (2022) v000, 2022, http://dx.doi.org/10.25950/cfa6938b, OpenKIM.

[379] B.-J. Lee, A modified embedded-atom method interatomic potential for the Fe–C system, Acta Mater. 54 (3) (2006) 701–711.
[380] G.J. Ackland, D.J. Bacon, A.F. Calder, T. Harry, Computer simulation of point defect properties in dilute Fe-Cu alloy using a many-body interatomic potential, Phil. Mag. A 75 (3) (1997) 713–732.
[381] S. Starikov, D. Smirnova, T. Pradhan, Y. Lysogorskiy, H. Chapman, M. Mrovec, R. Drautz, Angular-dependent interatomic potential for large-scale atomistic simulation of iron: Development and comprehensive comparison with existing interatomic models, Phys. Rev. Mater. 5 (2021) 063607.
[382] B.-J. Lee, M. Baskes, H. Kim, Y.K. Cho, Second nearest-neighbor modified embedded atom method potentials for bcc transition metals, Phys. Rev. B 64 (18) (2001) 184102.
[383] B.-J. Lee, J.-W. Jang, MEAM potential for the Fe-H system developed by Lee and Jang (2007) v001, 2021, http://dx.doi.org/10.25950/94b6e36f, OpenKIM.
[384] H. Chamati, N. Papanicolaou, Y. Mishin, D. Papaconstantopoulos, Embedded-atom potential for Fe and its application to self-diffusion on Fe(100), Surf. Sci. 600 (9) (2006) 1793–1803.
[385] S.M. Eich, D. Beinke, G. Schmitz, EAM/TBM potential for Fe-Cr developed by Eich et al. (2015) v000, 2021, http://dx.doi.org/10.25950/345ef364, OpenKIM.
[386] S.-A. Etesami, E. Asadi, MEAM potential for Fe developed by Etesami and Asadi (2018) v001, 2021, http://dx.doi.org/10.25950/baf36665, OpenKIM.
[387] M.-C. Marinica, F. Willaime, J.-P. Crocombette, Irradiation-induced formation of nanocrystallites with $C15$ laves phase structure in bcc iron, Phys. Rev. Lett. 108 (2012) 025501.
[388] S.L. Dudarev, P.M. Derlet, Erratum: A 'magnetic' interatomic potential for molecular dynamics simulations, J. Phys.: Condens. Matter 19 (23) (2007) 239001.
[389] B.-J. Lee, J.-W. Jang, A modified embedded-atom method interatomic potential for the Fe–H system, Acta Mater. 55 (20) (2007) 6779–6788.
[390] X. Zhou, EAM potential (LAMMPS cubic hermite tabulation) for Fe developed by Zhou, Johnson and Wadley (2004) v005, 2018, http://dx.doi.org/10.25950/5c98ab8c, OpenKIM.
[391] W.-M. Choi, Y. Kim, D. Seol, B.-J. Lee, MEAM potential for the Co-Fe system developed by Choi et al. (2017) v001, 2021, http://dx.doi.org/10.25950/f2666396, OpenKIM.
[392] S. Starikov, D. Smirnova, T. Pradhan, Y. Lysogorskiy, M. Mrovec, R. Drautz, LAMMPS ADP potential for Fe developed by Starikov et al. (2021) v000, 2022, http://dx.doi.org/10.25950/69dfec96, OpenKIM.
[393] M.I. Mendelev, EAM potential (LAMMPS cubic hermite tabulation) for Fe developed by Mendelev et al. (2003); Potential #2 v005, 2018, http://dx.doi.org/10.25950/f3e7b22d, OpenKIM.
[394] E. Tadmor, EAM potential (LAMMPS cubic hermite tabulation) for Fe developed by Zhou, Johnson, and Wadley (2004); NIST retabulation v000, 2018, http://dx.doi.org/10.25950/f44e9af3, OpenKIM.
[395] B.-J. Lee, J.-H. Shim, H.M. Park, A semi-empirical atomic potential for the Fe-Cr binary system, CALPHAD 25 (4) (2001) 527–534.
[396] S.-Y. Kim, Modified Johnson pair potential for Fe developed by Morris, Aga, and Levashov (2008) v003, 2018, http://dx.doi.org/10.25950/e8fbaf89, OpenKIM.
[397] E. Asadi, M.A. Zaeem, S. Nouranian, M.I. Baskes, MEAM potential for Fe developed by Asadi et al. (2015) v001, 2021, http://dx.doi.org/10.25950/ffb5e974, OpenKIM.
[398] E. Asadi, M.A. Zaeem, S. Nouranian, M.I. Baskes, Quantitative modeling of the equilibration of two-phase solid-liquid Fe by atomistic simulations on diffusive time scales, Phys. Rev. B 91 (2015) 024105.
[399] T. Brink, M. Müller, P. Erhart, K. Albe, Tersoff-style three-body potential for bcc and fcc Fe developed by Muller, Erhart, and Albe (2007) v004, 2021, http://dx.doi.org/10.25950/b7f56ed7, OpenKIM.
[400] B.-J. Lee, J.-H. Shim, H.M. Park, MEAM potential for the Fe-Cr system developed by Lee, Shim and Park (2001) v000, 2022, http://dx.doi.org/10.25950/d9ecb4ef, OpenKIM.
[401] M.I. Mendelev, Finnis–Sinclair potential (LAMMPS cubic hermite tabulation) for the V-Fe system developed by Mendelev et al. (2007) v005, 2018, http://dx.doi.org/10.25950/8b792449, OpenKIM.
[402] L. Proville, D. Rodney, M.-C. Marinica, Quantum effect on thermally activated glide of dislocations, Nature Mater. 11 (2012) 845–849.
[403] M. Wen, Modified Stillinger–Weber potential (MX2) for monolayer MoS2 developed by Wen et al. (2017) v001, 2018, http://dx.doi.org/10.25950/eeedbbc4, OpenKIM.
[404] Y. Zuo, A spectral neighbor analysis potential for Mo developed by Yunxing Zuo v000, 2020, http://dx.doi.org/10.25950/6b5dc6c4, OpenKIM.
[405] Y. Zuo, A quadratic spectral neighbor analysis potential for Mo developed by Yunxing Zuo v000, 2020, http://dx.doi.org/10.25950/a52c3237, OpenKIM.
[406] P.M. Derlet, D. Nguyen-Manh, S.L. Dudarev, Multiscale modeling of crowdion and vacancy defects in body-centered-cubic transition metals, Phys. Rev. B 76 (2007) 054107.
[407] M. Wen, S.N. Shirodkar, P. Plecháč, E. Kaxiras, R.S. Elliott, E.B. Tadmor, A force-matching Stillinger–Weber potential for MoS2: Parameterization and Fisher information theory based sensitivity analysis, J. Appl. Phys. 122 (24) (2017) 244301.
[408] B.-J. Lee, M.I. Baskes, H. Kim, Y.K. Cho, MEAM potential for Mo developed by Lee et al. (2001) v000, 2022, http://dx.doi.org/10.25950/e342424c, OpenKIM.
[409] R.S. Elliott, Morse potential (shifted) for Mo by Girifalco and Weizer (1959) using a low-accuracy cutoff distance v004, 2020, http://dx.doi.org/10.25950/4d9a28e6, OpenKIM.
[410] M.R. Gilbert, EAM potential (magnetic, cubic tabulation) for Mo developed by Derlet, Nguyen-Manh and Dudarev (2007) v002, 2018, http://dx.doi.org/10.25950/2afad7cc, OpenKIM.
[411] X. Zhang, H.T. Nguyen, Tersoff potentials for large deformation pathways and fracture of MoSe2 v001, 2021, http://dx.doi.org/10.25950/78b6b863, OpenKIM.
[412] X. Li, A spectral neighbor analysis potential for Nb-Mo-Ta-W developed by Xiangguo Li (2019) v000, 2020, http://dx.doi.org/10.25950/c34c3362, OpenKIM.
[413] C. Chen, Z. Deng, R. Tran, H. Tang, I.-H. Chu, S.P. Ong, Accurate force field for molybdenum by machine learning large materials data, Phys. Rev. Mater. 1 (4) (2017) 043603.
[414] H. Park, M.R. Fellinger, T.J. Lenosky, W.W. Tipton, D.R. Trinkle, S.P. Rudin, C. Woodward, J.W. Wilkins, R.G. Hennig, Ab initio based empirical potential used to study the mechanical properties of molybdenum, Phys. Rev. B 85 (2012) 214121.
[415] Y. Zuo, C. Chen, X. Li, Z. Deng, Y. Chen, J. Behler, G. Csányi, A.V. Shapeev, A.P. Thompson, M.A. Wood, et al., Performance and cost assessment of machine learning interatomic potentials, J. Phys. Chem. A 124 (4) (2020) 731–745.
[416] C. Chen, A spectral neighbor analysis potential for Mo developed by Chi Chen (2019) v000, 2020, http://dx.doi.org/10.25950/63ad82cb, OpenKIM.
[417] Y. Kurniawan, C. Petrie, K. Williams, M.K. Transtrum, R.S. Elliott, E.B. Tadmor, D.S. Karls, M. Wen, Modified Stillinger–Weber potential (MX2) for monolayer MoS2 by Kurniawan et al. (2022) v000, 2022, http://dx.doi.org/10.25950/328bfabb, OpenKIM.
[418] J.-S. Kim, D. Seol, J. Ji, H.-S. Jang, B.-J. Lee, MEAM potential for the Pt-Mo system developed by Kim and Lee (2017) v001, 2021, http://dx.doi.org/10.25950/e982a9fd, OpenKIM.
[419] H. Park, M. Fellinger, T. Lenosky, W.W. Tipton, D.R. Trinkle, S.P. Rudin, C. Woodward, R.G. Hennig, MEAM potential for Mo developed by Park et al. (2012) v001, 2021, http://dx.doi.org/10.25950/e95f5785, OpenKIM.
[420] S. Starikov, L. Kolotova, A. Kuksin, D. Smirnova, V. Tseplyaev, Atomistic simulation of cubic and tetragonal phases of U-Mo alloy: Structure and thermodynamic properties, J. Nucl. Mater. 499 (2018) 451–463.
[421] M. Wen, Stillinger–Weber model driver for monolayer MX2 systems v001, 2018, http://dx.doi.org/10.25950/7d664757, OpenKIM.
[422] R.S. Elliott, Morse potential (shifted) for Mo by Girifalco and Weizer (1959) using a high-accuracy cutoff distance v004, 2020, http://dx.doi.org/10.25950/42b4b4c6, OpenKIM.
[423] R.S. Elliott, Morse potential (shifted) for Mo by Girifalco and Weizer (1959) using a medium-accuracy cutoff distance v004, 2020, http://dx.doi.org/10.25950/52b2a5ba, OpenKIM.
[424] G.-U. Jeong, C.S. Park, H.-S. Do, S.-M. Park, B.-J. Lee, MEAM potential for the Pd-Mo system developed by Jeong et al. (2018) v001, 2021, http://dx.doi.org/10.25950/4562ee5b, OpenKIM.
[425] Y. Kurniawan, C.L. Petrie, K.J. Williams, M.K. Transtrum, E.B. Tadmor, R.S. Elliott, D.S. Karls, M. Wen, Bayesian, frequentist, and information geometry approaches to parametric uncertainty quantification of classical empirical interatomic potentials, 2021.
[426] X.-G. Li, C. Chen, H. Zheng, Y. Zuo, S.P. Ong, Complex strengthening mechanisms in the NbMoTaW multi-principal element alloy, npj Comput. Mater. 6 (2020).
[427] R.E. Miller, LAMMPS ADP potential for the U-Mo system developed by Starikov et al. (2017) v000, 2019, http://dx.doi.org/10.25950/466f25ce, OpenKIM.
[428] B. Runnels, D.S. Karls, B. Waters, Relaxed energy as a function of tilt angle for a 100 symmetric tilt grain boundary in fcc Al v003, 2022, OpenKIM, https://openkim.org/cite/TE_918853243284_003.
[429] B. Runnels, D.S. Karls, B. Waters, Relaxed energy as a function of tilt angle for a 110 symmetric tilt grain boundary in fcc Al v001, 2022, OpenKIM, https://openkim.org/cite/TE_202986963854_001.
[430] B. Runnels, D.S. Karls, B. Waters, Relaxed energy as a function of tilt angle for a 111 symmetric tilt grain boundary in fcc Al v001, 2022, OpenKIM, https://openkim.org/cite/TE_117904176283_001.
[431] B. Runnels, D.S. Karls, B. Waters, Relaxed energy as a function of tilt angle for a 112 symmetric tilt grain boundary in fcc Al v001, 2022, OpenKIM, https://openkim.org/cite/TE_641102822364_001.
[432] B. Runnels, D.S. Karls, B. Waters, Relaxed energy as a function of tilt angle for a 100 symmetric tilt grain boundary in fcc Cu v001, 2022, OpenKIM, https://openkim.org/cite/TE_529988253259_001.
[433] B. Runnels, D.S. Karls, B. Waters, Relaxed energy as a function of tilt angle for a 110 symmetric tilt grain boundary in fcc Cu v001, 2022, OpenKIM, https://openkim.org/cite/TE_708214008908_001.
[434] B. Runnels, D.S. Karls, B. Waters, Relaxed energy as a function of tilt angle for a 111 symmetric tilt grain boundary in fcc Cu v001, 2022, OpenKIM, https://openkim.org/cite/TE_603516505525_001.
[435] B. Runnels, D.S. Karls, B. Waters, Relaxed energy as a function of tilt angle for a 112 symmetric tilt grain boundary in fcc Cu v001, 2022, OpenKIM, https://openkim.org/cite/TE_288691353820_001.

[436] B. Runnels, D.S. Karls, B. Waters, Relaxed energy as a function of tilt angle for a 100 symmetric tilt grain boundary in fcc Ni v001, 2022, OpenKIM, https://openkim.org/cite/TE_457754988992_001.
[437] B. Runnels, D.S. Karls, B. Waters, Relaxed energy as a function of tilt angle for a 110 symmetric tilt grain boundary in fcc Ni v001, 2022, OpenKIM, https://openkim.org/cite/TE_980409230161_001.
[438] B. Runnels, D.S. Karls, B. Waters, Relaxed energy as a function of tilt angle for a 111 symmetric tilt grain boundary in fcc Ni v001, 2022, OpenKIM, https://openkim.org/cite/TE_035582886963_001.
[439] B. Runnels, D.S. Karls, B. Waters, Relaxed energy as a function of tilt angle for a 112 symmetric tilt grain boundary in fcc Ni v001, 2022, OpenKIM, https://openkim.org/cite/TE_893686795562_001.
[440] B. Runnels, D.S. Karls, B. Waters, Relaxed energy as a function of tilt angle for a 100 symmetric tilt grain boundary in fcc Fe v001, 2022, OpenKIM, https://openkim.org/cite/TE_814353485766_001.
[441] B. Runnels, D.S. Karls, B. Waters, Relaxed energy as a function of tilt angle for a 110 symmetric tilt grain boundary in fcc Fe v001, 2022, OpenKIM, https://openkim.org/cite/TE_729107030375_001.
[442] B. Runnels, D.S. Karls, B. Waters, Relaxed energy as a function of tilt angle for a 111 symmetric tilt grain boundary in fcc Fe v001, 2022, OpenKIM, https://openkim.org/cite/TE_989116099275_001.
[443] B. Runnels, D.S. Karls, B. Waters, Relaxed energy as a function of tilt angle for a 112 symmetric tilt grain boundary in fcc Fe v001, 2022, OpenKIM, https://openkim.org/cite/TE_317621478872_001.
[444] B. Runnels, D.S. Karls, B. Waters, Relaxed energy as a function of tilt angle for a 100 symmetric tilt grain boundary in bcc Fe v001, 2022, OpenKIM, https://openkim.org/cite/TE_175540441720_001.
[445] B. Runnels, D.S. Karls, B. Waters, Relaxed energy as a function of tilt angle for a 110 symmetric tilt grain boundary in bcc Fe v001, 2022, OpenKIM, https://openkim.org/cite/TE_558145380113_001.
[446] B. Runnels, D.S. Karls, B. Waters, Relaxed energy as a function of tilt angle for a 111 symmetric tilt grain boundary in bcc Fe v001, 2022, OpenKIM, https://openkim.org/cite/TE_752424681735_001.
[447] B. Runnels, D.S. Karls, B. Waters, Relaxed energy as a function of tilt angle for a 112 symmetric tilt grain boundary in bcc Fe v001, 2022, OpenKIM, https://openkim.org/cite/TE_187984704771_001.
[448] B. Runnels, D.S. Karls, B. Waters, Relaxed energy as a function of tilt angle for a 100 symmetric tilt grain boundary in bcc Mo v001, 2022, OpenKIM, https://openkim.org/cite/TE_529178526487_001.
[449] B. Runnels, D.S. Karls, B. Waters, Relaxed energy as a function of tilt angle for a 110 symmetric tilt grain boundary in bcc Mo v001, 2022, OpenKIM, https://openkim.org/cite/TE_671775543629_001.
[450] B. Runnels, D.S. Karls, B. Waters, Relaxed energy as a function of tilt angle for a 111 symmetric tilt grain boundary in bcc Mo v001, 2022, OpenKIM, https://openkim.org/cite/TE_107990591816_001.
[451] B. Runnels, D.S. Karls, B. Waters, Relaxed energy as a function of tilt angle for a 112 symmetric tilt grain boundary in bcc Mo v001, 2022, OpenKIM, https://openkim.org/cite/TE_568499993431_001.
[452] S.M. Foiles, M.I. Baskes, M.S. Daw, Embedded-atom-method functions for the fcc metals Cu, Ag, Au, Ni, Pd, Pt, and their alloys, Phys. Rev. B 33 (1986) 7983–7991.
[453] S. Plimpton, Fast parallel algorithms for short-range molecular dynamics, J. Comput. Phys. 117 (1) (1995) 1–19.
[454] R.S. Elliott, E.B. Tadmor, Knowledgebase of interatomic models (KIM) application programming interface (API), 2011, OpenKIM, https://openkim.org/kim-api.
[455] J.D. Honeycutt, H.C. Andersen, Molecular dynamics study of melting and freezing of small lennard-jones clusters, J. Phys. Chem. 91 (19) (1987) 4950–4963.
[456] A. Stukowski, Visualization and analysis of atomistic simulation data with OVITO—the Open Visualization Tool, Modelling Simul. Mater. Sci. Eng. 18 (1) (2010) 015012, Software available at http://ovito.org.
[457] D. Schopf, EAM potential (IMD tabulation) for the Al-Mn-Pd system developed by Schopf et al. (2012) v003, 2018, http://dx.doi.org/10.25950/769f29cf, OpenKIM.
[458] D. Schopf, P. Brommer, B. Frigan, H.-R. Trebin, Embedded atom method potentials for Al-Pd-Mn phases, Phys. Rev. B 85 (2012) 054201.
[459] B. Runnels, I.J. Beyerlein, S. Conti, M. Ortiz, A relaxation method for the energy and morphology of grain boundaries and interfaces, J. Mech. Phys. Solids (2015).
[460] B. Runnels, A model for energy and morphology of crystalline grain boundaries with arbitrary geometric character (Ph.D. thesis), California Institute of Technology, 2016.
[461] C. Tebaldi, R. Knutti, The use of the multi-model ensemble in probabilistic climate projections, Phil. Trans. R. Soc. A 365 (1857) (2007) 2053–2075.
[462] F. Giorgi, L.O. Mearns, Calculation of average, uncertainty range, and reliability of regional climate changes from AOGCM simulations via the "Reliability Ensemble Averaging" (REA) method, J. Clim. 15 (10) (2002) 1141–1158.
[463] P.R. Cantwell, T. Frolov, T.J. Rupert, A.R. Krause, C.J. Marvel, G.S. Rohrer, J.M. Rickman, M.P. Harmer, Grain boundary complexion transitions, Annu. Rev. Mater. Res 50 (1) (2020) 465–492.
[464] A.B. Mazitov, A.R. Oganov, Grain boundaries in minerals: atomic structure, phase transitions, and effect on strength of polycrystals, 2021, arXiv preprint arXiv:2106.13570.
[465] M. Guziewski, A.D. Banadaki, S. Patala, S.P. Coleman, Application of Monte Carlo techniques to grain boundary structure optimization in silicon and silicon-carbide, Comput. Mater. Sci. 182 (2020) 109771.
[466] J. Towns, T. Cockerill, M. Dahan, I. Foster, K. Gaither, A. Grimshaw, V. Hazlewood, S. Lathrop, D. Lifka, G.D. Peterson, R. Roskies, J.R. Scott, N. Wilkins-Diehr, XSEDE: Accelerating scientific discovery, Comput. Sci. Eng. 16 (5) (2014) 62–74.